



# Chronicling the Host Galaxy Properties of the Remarkable Repeating FRB 20201124A

Wen-fai Fong<sup>1</sup>, Yuxin Dong<sup>1,2</sup>, Joel Leja<sup>3,4,5</sup>, Shivani Bhandari<sup>6</sup>, Cherie K. Day<sup>6,7</sup>, Adam T. Deller<sup>7</sup>,  
Pravir Kumar<sup>7</sup>, J. Xavier Prochaska<sup>8,9</sup>, Danica R. Scott<sup>10</sup>, Keith W. Bannister<sup>6</sup>, Tarraneh Eftekhari<sup>11</sup>,  
Alexa C. Gordon<sup>1</sup>, Kasper E. Heintz<sup>12,13</sup>, Clancy W. James<sup>10</sup>, Charles D. Kilpatrick<sup>1</sup>, Elizabeth K. Mahony<sup>6</sup>,  
Alicia Rouco Escorial<sup>1</sup>, Stuart D. Ryder<sup>14,15</sup>, Ryan M. Shannon<sup>7</sup>, and Nicolas Tejos<sup>16</sup>

<sup>1</sup> Center for Interdisciplinary Exploration and Research in Astrophysics (CIERA) and Department of Physics and Astronomy, Northwestern University, Evanston, IL 60208, USA; [wfong@northwestern.edu](mailto:wfong@northwestern.edu)

<sup>2</sup> Purdue University, Department of Physics and Astronomy, 525 Northwestern Avenue, West Lafayette, IN 47907, USA

<sup>3</sup> Department of Astronomy & Astrophysics, The Pennsylvania State University, University Park, PA 16802, USA

<sup>4</sup> Institute for Computational & Data Sciences, The Pennsylvania State University, University Park, PA 16802, USA

<sup>5</sup> Institute for Gravitation and the Cosmos, The Pennsylvania State University, University Park, PA 16802, USA

<sup>6</sup> CSIRO, Space and Astronomy, PO Box 76, Epping, NSW 1710, Australia

<sup>7</sup> Centre for Astrophysics and Supercomputing, Swinburne University of Technology, Hawthorn, VIC 3122, Australia

<sup>8</sup> Department of Astronomy and Astrophysics, University of California, Santa Cruz, CA 95064, USA

<sup>9</sup> Kavli Institute for the Physics and Mathematics of the Universe (Kavli IPMU), 5-1-5 Kashiwanoha, Kashiwa, 277-8583, Japan

<sup>10</sup> International Centre for Radio Astronomy Research, Curtin University, Bentley, WA 6102, Australia

<sup>11</sup> Center for Astrophysics | Harvard & Smithsonian, 60 Garden Street, Cambridge, MA 02138, USA

<sup>12</sup> Centre for Astrophysics and Cosmology, Science Institute, University of Iceland, Dunhagi 5, 107 Reykjavík, Iceland

<sup>13</sup> Cosmic Dawn Center (DAWN), Niels Bohr Institute, University of Copenhagen, Jagtvej 128, DK-2100 Copenhagen O, Denmark

<sup>14</sup> Department of Physics & Astronomy, Macquarie University, Sydney, NSW 2109, Australia

<sup>15</sup> Macquarie University, Research Centre for Astronomy, Astrophysics & Astrophotonics, Sydney, NSW 2109, Australia

<sup>16</sup> Instituto de Física, Pontificia Universidad Católica de Valparaíso, Casilla 4059, Valparaíso, Chile

Received 2021 June 22; revised 2021 August 15; accepted 2021 August 31; published 2021 September 30

## Abstract

We present the Australian Square Kilometre Array Pathfinder localization and follow-up observations of the host galaxy of the repeating fast radio burst (FRB) source, FRB 20201124A, the fifth such extragalactic repeating FRB with an identified host. From spectroscopic observations using the 6.5 m MMT Observatory, we derive a redshift  $z = 0.0979 \pm 0.0001$ , a star formation rate inferred from H $\alpha$  emission  $\text{SFR}(\text{H}\alpha) \approx 2.1 M_{\odot} \text{ yr}^{-1}$ , and a gas-phase metallicity of  $12 + \log(\text{O}/\text{H}) \approx 9.0$ . By jointly modeling the 12 filter optical–mid-infrared (MIR) photometry and spectroscopy of the host, we infer a median stellar mass of  $\sim 2 \times 10^{10} M_{\odot}$ , internal dust extinction  $A_V \approx 1\text{--}1.5$  mag, and a mass-weighted stellar population age of  $\sim 5\text{--}6$  Gyr. Connecting these data to the radio and X-ray observations, we cannot reconcile the broadband behavior with strong active galactic nucleus activity and instead attribute the dominant source of persistent radio emission to star formation, likely originating from the circumnuclear region of the host. The modeling also indicates a hot dust component contributing to the MIR luminosity at a level of  $\sim 10\%\text{--}30\%$ . We model the host galaxy’s star formation and mass assembly histories, finding that the host assembled  $>90\%$  of its mass by 1 Gyr ago and exhibited a fairly constant SFR for most of its existence, with no clear evidence of past starburst activity.

*Unified Astronomy Thesaurus concepts:* [Radio transient sources \(2008\)](#); [Radio bursts \(1339\)](#); [Star formation \(1569\)](#); [Stellar populations \(1622\)](#); [Neutron stars \(1108\)](#)

*Supporting material:* data behind figure

## 1. Introduction

Fast radio bursts (FRBs) are bright, millisecond-duration pulses detected almost exclusively at  $\sim 0.1\text{--}8$  GHz frequencies (Lorimer et al. 2007; Thornton et al. 2013; Gajjar et al. 2018; Cordes & Chatterjee 2019; Petroff et al. 2019; The CHIME/FRB Collaboration et al. 2021). Perhaps their most enigmatic feature is that a fraction are observed to undergo repeat bursts from the same source (“repeaters”; Spitler et al. 2016), while the vast majority have not been observed to repeat (apparent “nonrepeaters” or “one-off” bursts; Shannon et al. 2018). It is not yet clear whether the collective population of FRBs originates from a single type of stellar progenitor or from multiple channels (Cordes & Chatterjee 2019; Platts et al. 2019). However, population studies indicate that bursts from repeating FRBs are observed to have narrow bandwidths and longer temporal durations than those of apparent nonrepeaters (Gajjar et al. 2018; CHIME/FRB Collaboration et al. 2019; Day et al. 2020; Fonseca et al. 2020; Pleunis et al. 2021).

Beyond these attributes, scant clues exist for differences in their physical origins.

Alongside studies of their emission properties, examining the environments of FRBs on subparsec to kiloparsec scales can be equally informative. Thus far, only a fraction of known extragalactic repeating FRBs have been localized to host galaxies (Chatterjee et al. 2017; Tendulkar et al. 2017; Marcote et al. 2020; Macquart et al. 2020; Heintz et al. 2020; Bhandari et al. 2021; Bhardwaj et al. 2021a, 2021b; Li et al. 2021).<sup>17</sup> Much closer by, FRB-like emission has been detected from a Milky Way magnetar, SGR 1935 + 2154 (CHIME/FRB Collaboration et al. 2020; Bochenek et al. 2020). All identified repeating FRB hosts have evidence for low to modest ongoing star formation rates of  $\sim 0.06\text{--}2 M_{\odot} \text{ yr}^{-1}$  (Gordon et al. 2004; Bhandari et al. 2020a; Heintz et al. 2020), several exhibit spiral

<sup>17</sup> FRB 20201124A is the fifth announced repeating FRB with a host galaxy. In total, there are eight such FRB sources known as of 2021 August.

arm morphologies (Bhardwaj et al. 2021a; Mannings et al. 2021; Tendulkar et al. 2021), and their stellar populations span a range of stellar masses,  $\sim 10^8 - 10^{10.5} M_\odot$  (de Blok et al. 2008; Bhandari et al. 2020a; Heintz et al. 2020; Mannings et al. 2021). At face value, these characteristics, coupled with the absence of any quiescent host galaxy identifications for repeating FRBs, may indicate that FRBs are connected to host galaxies with ongoing star formation. However, studies of their more local environments reveal a rich diversity. For instance, the discovery of the repeating FRB 20200120E in an old (9.1 Gyr) globular cluster on the outskirts of the grand design spiral galaxy M81 (Bhardwaj et al. 2021a; Kirsten et al. 2021a) and the detection of the repeating FRB 20121102A embedded in a star-forming knot in its dwarf host galaxy (Bassa et al. 2017) seemingly represent polar opposite local environments. If all repeaters discovered to date originate from the same type of progenitor, then the progenitor model must accommodate the observed diversity of both local and galactic environments. Additionally, any connection in progenitors to the population of apparent nonrepeaters remains opaque.

The number of repeating FRBs with identified hosts are still few in number. We are thus motivated to characterize the environments of any new repeating FRBs to understand the full spectrum of environments that give rise to these events. FRB 20201124A was first discovered by the Canadian Hydrogen Intensity Mapping Experiment FRB (CHIME/FRB) collaboration (CHIME/FRB Collaboration 2021a, 2021b) on 2020 November 24 UTC 08:50:41. On 2021 March 31, the CHIME/FRB collaboration reported that the FRB 20201124A source had repeated and was entering a period of high activity (CHIME/FRB Collaboration 2021a). Numerous radio facilities have since reported the detection of repeating bursts from the same source, including the Australian Square Kilometre Array Pathfinder (ASKAP; Kumar et al. 2021b, 2021a), the Five-hundred-meter Aperture Spherical radio Telescope (FAST; Xu et al. 2021), the Very Large Array (VLA; Law et al. 2021), the Upgraded Giant Metrewave Radio Telescope (uGMRT; Wharton et al. 2021a; Marthi et al. 2021), the Stockert 25 m Radio Telescope (Herrmann 2021), Onsala Space Observatory (Kirsten et al. 2021b), and the Allen Telescope Array (Farah et al. 2021). To date, over 1700 bursts from the FRB 20201124A source have been reported between its discovery on 2020 November 24 to 2021 August 10<sup>18</sup>. In addition, uGMRT and VLA observations uncovered a persistent radio source (PRS) at 650 MHz, 3 GHz, and 9 GHz (Wharton et al. 2021b; Ravi et al. 2021; Ricci et al. 2021) reported to be unresolved on arcsecond scales.

Here, we report on the arcsecond-precision localization based on three bursts from the actively repeating FRB 20201124A source detected by the ASKAP telescope as part of the Commensal Real-time ASKAP Fast Transients (CRAFT) project (Macquart et al. 2010). In Section 2, we describe the community observations to date and introduce the properties and localization of three ASKAP bursts, as well as their joint localization. Here, we also describe the follow-up observations of the host galaxy. In Section 3, we model the properties of the host galaxy, construct its star formation and mass assembly histories, and explore the origin of the persistent radio emission by connecting the broadband observations. In

Section 4, we discuss the host of FRB 20201124A in the context of other repeating FRB environments and the implications for the progenitors. We summarize in Section 5. We note that Ravi et al. (2021) and Piro et al. (2021) present independent analyses of the host galaxy and persistent radio emission of this FRB, and our results are broadly consistent with those works.

Unless otherwise stated, all observations are reported in the AB magnitude system and have been corrected for Galactic extinction in the direction of the FRB using  $A_V = 1.95$  mag (Fitzpatrick & Massa 2007) and the Cardelli et al. (1989) extinction law. We employ a standard cosmology of  $H_0 = 69.6 \text{ km s}^{-1} \text{ Mpc}^{-1}$ ,  $\Omega_M = 0.286$  (Bennett et al. 2014), and  $\Omega_\lambda = 1 - \Omega_M = 0.714$ .

## 2. Observations and Burst Properties

### 2.1. ASKAP Burst Detections and Localization

We have been conducting surveys for FRBs with the ASKAP as part of the CRAFT project. ASKAP is a 36 antenna array, with each antenna equipped with a phased-array receiver capable of forming 36 beams on the sky for a total field of view of  $\sim 30 \text{ deg}^2$ . FRB searches are currently conducted on the incoherent sum of total intensities for each beam from each antenna. The searches reported here were conducted on data with 1.2 ms time resolution, 1 MHz spectral resolution, and a total bandwidth of 336 MHz. The data were recorded at a central frequency of either 864.5 MHz (low-band) or 1271.5 MHz (mid-band) on the incoherent sum of 23 or 24 antennas. The searches were initially conducted with the central ASKAP beam pointed at the best-fit position of the initial CHIME localization<sup>19</sup> (CHIME/FRB Collaboration 2021a). The ASKAP interferometric position for the burst, which differed by  $\sim 8$  arcminutes from the initial pointing, was used for observations of subsequent bursts after it had been measured.

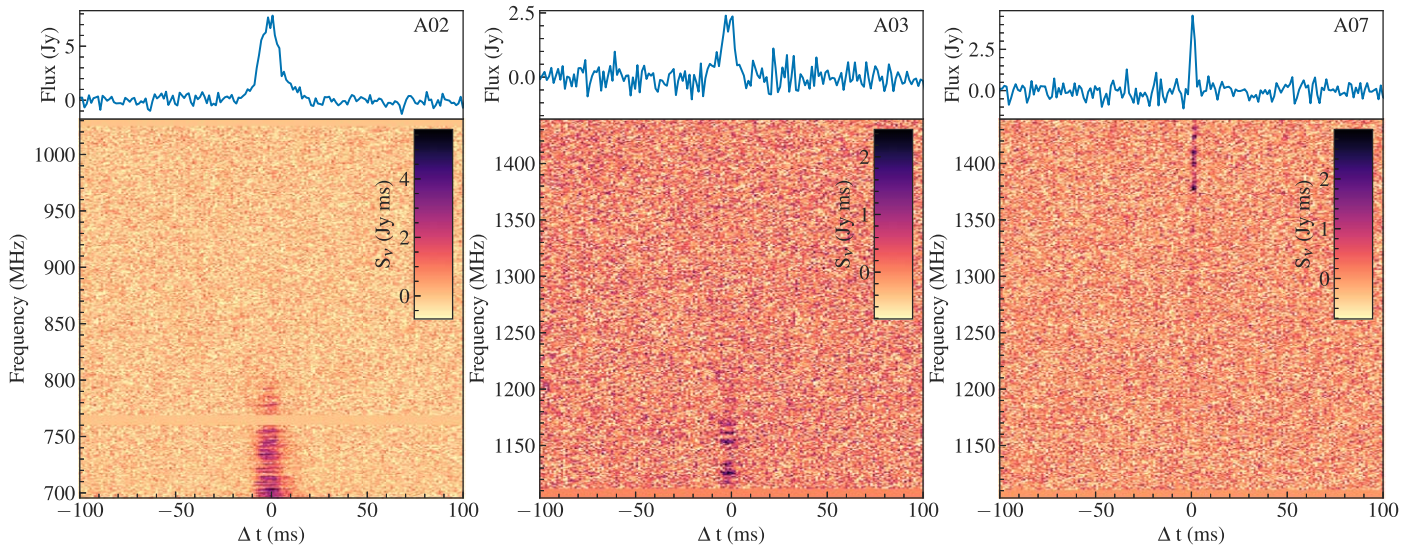
The searches were conducted in real time using a graphical processing unit-accelerated implementation (Bannister et al. 2019a) of the fast dispersion measure transform (Zackay & Ofek 2017), optimized for low latency (subsecond) detections. Further details of the search methods can be found in Bannister et al. (2019b). Candidates identified by the pipeline trigger a download of the 3.1 s duration voltage buffer for the candidate beam from each antenna. These voltages are correlated, calibrated, and imaged to interferometrically determine the position of the burst, following the procedure in Day et al. (2020).

Between 2021 April 1 and April 7 UTC, ASKAP detected 11 bursts from the FRB 20201124A source. For five of the bursts, real-time triggers were generated that led to the download of the voltage buffers that are required for localization.<sup>20</sup> From the five real-time triggers, two downloads experienced a partial networking failure that led to a reduced subset of antenna voltages being acquired (7 and 11, respectively). While the FRB itself could still be detected in the resultant images, the reduced sensitivity meant that the background continuum radio

<sup>19</sup> Searches were conducted with both hexagonal close pack and square beam arrangements. At 864.5 MHz, the beams were separated by 1.05 deg. At 1271.5 MHz, the beams were separated by 0.9 deg.

<sup>20</sup> Of the other six bursts, several were identified in real time but failed a temporal width test that prevents excessive download triggers caused by Radio Frequency Interference, while others were subthreshold and were only identified in the ex post facto analysis.

<sup>18</sup> Includes data from ATELS, Marthi et al. (2021), Piro et al. (2021), and the CHIME repeater catalog: <https://www.chime-frb.ca/repeaters/FRB20201124A>.



**Figure 1.** Dynamic spectra of three bursts detected by ASKAP from the FRB 2021124A source (A02, A03, and A07, from left to right). All bursts have been de-dispersed to their respective optimized DMs. In each subplot, the bottom panel shows the dynamic spectrum and the top panel shows the frequency-averaged pulse profile.

**Table 1**  
Properties of Three ASKAP Bursts from the FRB 2021124A Source

Date (UT)	TNS Name	Burst No.	Frequency (MHz)	Fluence (Jy ms)	DM ( $\text{pc cm}^{-3}$ )	R.A. (J2000)	Decl. (J2000)	$\sigma_{\text{maj}}$ (")	$\sigma_{\text{min}}$ (")	$\sigma_{\text{PA}}$ (deg)
2021-04-01	20210401A	A02	864.5	$187 \pm 12$	$412 \pm 3$	$05^{\text{h}}08^{\text{m}}03^{\text{s}}.48$	$+26^{\circ}03'38''.4$	1.3	0.7	140
2021-04-02	20210402A	A03	1271.5	$22 \pm 3$	$414 \pm 3$	$05^{\text{h}}08^{\text{m}}03^{\text{s}}.67$	$+26^{\circ}03'39''.5$	1.6	0.9	42
2021-04-04	20210404B	A07	1271.5	$11 \pm 2$	$414 \pm 3$	$05^{\text{h}}08^{\text{m}}03^{\text{s}}.55$	$+26^{\circ}03'39''.1$	1.1	0.7	13
Combined						$05^{\text{h}}08^{\text{m}}03^{\text{s}}.54$	$+26^{\circ}03'38''.4$	0.9	0.8	171

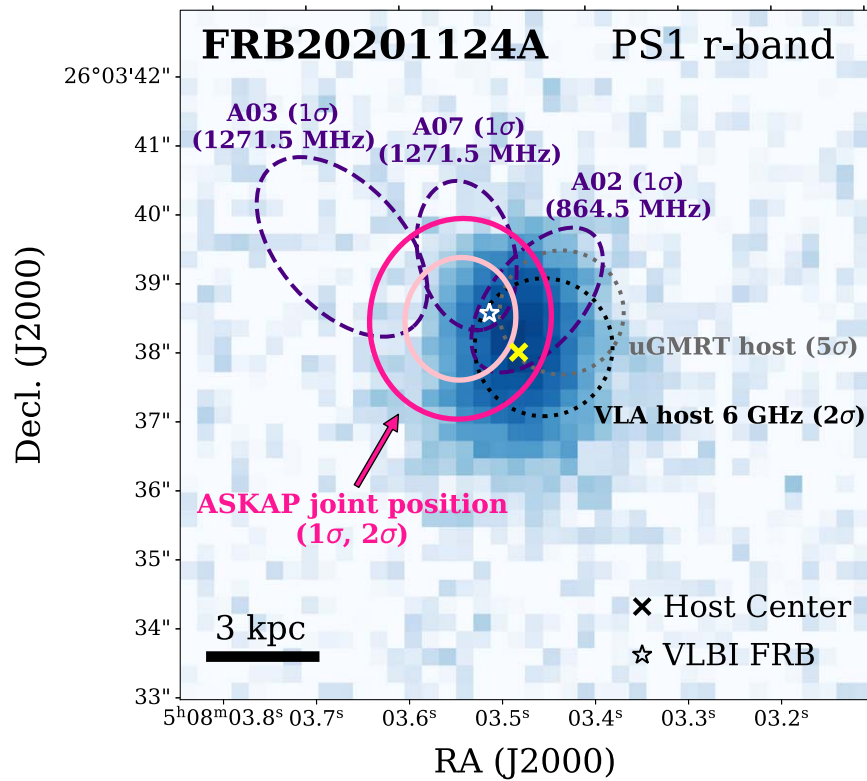
**Note.** Uncertainties correspond to  $1\sigma$  confidence. The terms  $\sigma_{\text{maj}}$  and  $\sigma_{\text{min}}$  are the uncertainties along the semimajor and semiminor axes, respectively, and then rotated by the  $\sigma_{\text{PA}}$ , defined as the position angle East of North.

sources used to refine the absolute astrometric calibration of the FRB image (described further below) could not be detected with a sufficiently high signal-to-noise ratio (S/N). This leaves three bursts suitable for localization. The results here are derived from the second, third, and seventh bursts detected by ASKAP (A02, A03, and A07), while the full set of burst properties will be described in an upcoming work. We previously reported on the localizations of the two bursts detected by ASKAP on 2021 April 1 and 2 UTC (FRB 20210401A: A02 and FRB 20210402A: A03, respectively; Day et al. 2021b, 2021a). Here, we also introduce the discovery and localization of a third burst detected by ASKAP on 2021 April 4 UTC (FRB 20210404B: A07). A02 was detected in the low-band at 864.5 MHz with a fluence of  $187 \pm 12$  Jy ms, while the latter two bursts were detected in the mid-band at 1271.5 MHz, with significantly lower fluences of  $22 \pm 3$  Jy ms and  $11 \pm 2$  Jy ms, respectively. The dispersion measure (DM) is  $\text{DM} = 412 \pm 3 \text{ pc cm}^{-3}$  (A02), and  $\text{DM} = 414 \pm 3 \text{ pc cm}^{-3}$  (A03 and A07), in agreement with the initial reported value from CHIME/FRB of  $\text{DM} = 413.52 \pm 0.05 \text{ pc cm}^{-3}$  (CHIME/FRB Collaboration 2021a). The burst dynamic spectra and frequency-averaged pulse profiles for the three bursts are displayed in Figure 1, and their properties are listed in Table 1. The spectral, temporal, and polarimetric properties of the bursts will be discussed in future papers.

While the FRB was strongly detected in every image, the absolute positional registration of the FRB images was

hampered by two issues: the low observing elevation at the time of A02 and A03 ( $\sim 20^{\circ}$ , which leads to a larger and much more elongated synthesized beam) and the paucity of bright background sources used to estimate and correct for any systematic position shift in the FRB image. The latter issue was particularly problematic in the mid-band (A03 and A07), due to the negative spectral index of typical background sources.

To account for the highly elongated synthesized beams, for each burst, we utilized a coordinate frame aligned with the position angle of the synthesized beam when estimating the systematic positional shift via a weighted mean of the positional offsets seen in the background radio sources. As each source utilized from the ASKAP image is consistent with being unresolved (any clearly resolved sources are rejected, as the position centroid at the ASKAP angular resolution/frequency may not match the position centroid used to calculate the catalog value) and hence has a position angle close to that of the synthesized beam, this approach leads to a minimal correlation in the offsets in the two coordinates. Day et al. (2021c) show that a simple weighted mean of the offsets obtained using background radio sources overestimates the accuracy to which the mean image shift can be determined when using images that are typical for ASKAP FRB detections, and determine that a scaling factor of 1.79 corrects for this on average. For A03 and A07, at elevations of  $\sim 20^{\circ}$ , however, we find that the uncertainty is likely still underestimated after the application of this scaling factor (based on the reduced  $\chi^2$  of the weighted mean of the offsets). An increased scale factor of



**Figure 2.** Archival Pan-STARRS1  $r$ -band imaging of the putative host galaxy of FRB 20201124A. The positions of the three bursts from ASKAP are plotted (purple dashed lines;  $1\sigma$ ), along with the joint probability map (solid pink contours;  $1\sigma$  and  $2\sigma$ , respectively). The ASKAP joint position is consistent within the  $1\sigma$  contour with the available Very Long Baseline Interferometry position (white star), and is  $\sim 1.3$  kpc offset from the measured center of the host galaxy (yellow ‘x’). Dotted lines denote the persistent radio emission positions reported by the VLA ( $2\sigma$ ; total error; Ravi et al. 2021) and uGMRT ( $5\sigma$ ; statistical uncertainty; Wharton et al. 2021b), which are nominally consistent with the host galaxy center and also consistent with the joint FRB position.

3 (rather than the global average of 1.79) yields a reduced  $\chi^2$  that is consistent with expectations for each individual FRB field, and so we conservatively use that for the systematic uncertainties that dominate the overall positional uncertainty shown in Table 1 and Figure 2.

We then place an improved constraint on the source position by evaluating the likelihood on a positional grid, using the probability from all three individual ASKAP localizations at each grid point. This results in a best-fit ASKAP position for the FRB of R.A. =  $05^{\text{h}}08^{\text{m}}03^{\text{s}}.54(5)$  and decl. =  $+26^{\circ}03'38''.4(9)$ , where the best-fit  $\chi^2$  was  $3.4^{\circ}$  for  $4^{\circ}$  of freedom and the uncertainties reflect 68% confidence intervals. The joint ASKAP localization is consistent with the reported Very Long Baseline Interferometry (VLBI) position (Marcote et al. 2021) within the 68% confidence contour, and the  $\chi^2$  indicates that despite the localization of burst A03 differing from the VLBI position by  $\sim 1.5\sigma$  in one coordinate, the uncertainties are overall well estimated. The positions and burst properties are listed in Table 1, and the positions are plotted in Figure 2.

## 2.2. Host Galaxy Association and Redshift Determination

The combined ASKAP position from FRB 20201124A is spatially consistent with the galaxy SDSS J050803.48 + 260338.0 (first reported in Day et al. 2021b) in the Sloan Digital Sky Survey (SDSS) catalog with tabulated photometric redshifts ( $z_{\text{phot}}$ ) of  $0.11 \pm 0.03$  and  $0.08 \pm 0.02$  from the Panoramic Survey Telescope and Rapid Response System Data Release 1 (Pan-STARRS DR1; Chambers et al. 2016; Beck et al. 2021) and SDSS Data Release 16 catalog (Ahumada et al. 2020), respectively.

Figure 2 shows an archival Pan-STARRS  $r$ -band image, along with the individual and joint ASKAP burst positions, the VLBI burst position, and the uGMRT and VLA PRS positions.

We use Source Extractor (Bertin & Arnouts 1996) on the Pan-STARRS  $r$ -band image to derive a host galaxy centroid of R.A. =  $05^{\text{h}}08^{\text{m}}03^{\text{s}}.477$ , decl. =  $+26^{\circ}03'37''.93$  with an uncertainty of  $\sim 11$ – $13$  mas in each coordinate. The best-fit projected angular offset between the centroid of the combined ASKAP position and the host center is  $\sim 0''.97$ , but the relatively low ASKAP localization precision for this source means that the FRB position cannot be excluded from consistency with the host centroid at a 95% confidence level. The VLBI position (Marcote et al. 2021), however, affords a highly precise measured offset from the host center of  $0.71 \pm 0''.03$ , taking into account the reported VLBI uncertainty, the host centroid uncertainty, and the median astrometric tie uncertainty of Pan-STARRS to Gaia of 22 mas (Magnier et al. 2020). Using the angular separation and the extinction-corrected magnitude,  $r \approx 17.84$  mag (Table 2), we calculate a low probability of chance coincidence,  $P_{\text{cc}} \approx 6.9 \times 10^{-5}$  (Bloom et al. 2002), pointing to a robust association.<sup>21</sup> This association is strengthened by adopting the Bayesian formalism PATH (Probabilistic Association of Transients to their Hosts; Aggarwal et al. 2021) and using the PS1 catalog to derive a posterior probability of association,  $P(O|x) \approx 0.997$  (where  $P(O|x) > 0.95$  may be considered a secure association), assuming a 10% prior probability that the host galaxy is not in the list of cataloged galaxies. For the PATH probability, we assume an

<sup>21</sup> We use Equation 1 in Berger (2010) with  $m = 17.84$  mag and  $\delta R = 0''.71$ .

**Table 2**  
FRB 20201124A Host Galaxy Photometry

Source	Filter/Band	$m_\lambda$ (AB mag)	$A_\lambda$ (mag)	$F_\nu$ ( $\mu\text{Jy}$ )	$\nu L_\nu$ ( $\text{erg s}^{-1}$ )
Swift/XRT	1.7 keV	...	...	$<0.0128$	$<1.28 \times 10^{42}$
SDSS	<i>u</i>	$19.974 \pm 0.545$	3.075	$37.1 \pm 24.2$	$(7.73 \pm 0.50) \times 10^{42}$
Pan-STARRS	<i>g</i>	$18.462 \pm 0.038$	2.276	$149.7 \pm 5.3$	$(2.29 \pm 0.08) \times 10^{43}$
Pan-STARRS	<i>r</i>	$17.904 \pm 0.029$	1.637	$250.2 \pm 6.8$	$(2.99 \pm 0.08) \times 10^{43}$
Pan-STARRS	<i>i</i>	$17.591 \pm 0.034$	1.186	$333.9 \pm 10.6$	$(3.27 \pm 0.10) \times 10^{43}$
Pan-STARRS	<i>z</i>	$17.419 \pm 0.028$	0.920	$391.2 \pm 10.2$	$(3.33 \pm 0.09) \times 10^{43}$
Pan-STARRS	<i>y</i>	$17.385 \pm 0.059$	0.759	$403.7 \pm 22.5$	$(3.09 \pm 0.17) \times 10^{43}$
2MASS	<i>J</i>	$16.964 \pm 0.119$	0.480	$594.5 \pm 68.9$	$(3.50 \pm 0.41) \times 10^{43}$
2MASS	<i>H</i>	$16.787 \pm 0.123$	0.283	$700.2 \pm 83.4$	$(3.12 \pm 0.37) \times 10^{43}$
2MASS	<i>K</i>	$16.707 \pm 0.115$	0.171	$753.7 \pm 84.2$	$(2.58 \pm 0.28) \times 10^{43}$
WISE	W1	$17.127 \pm 0.041$	0.075	$511.9 \pm 19.7$	$(1.12 \pm 0.04) \times 10^{43}$
WISE	W2	$17.443 \pm 0.048$	0.044	$382.7 \pm 17.3$	$(6.10 \pm 0.27) \times 10^{42}$
WISE	W3	$14.998 \pm 0.061$	0.013	$3637.5 \pm 210.2$	$(2.22 \pm 0.13) \times 10^{43}$
WISE	W4	$14.587 \pm 0.256$	0.007	$5311.3 \pm 1412.3$	$(1.76 \pm 0.47) \times 10^{43}$
uGMRT	650 MHz	...	...	$700 \pm 100$	$(1.12 \pm 0.16) \times 10^{38}$
VLA	1.4 GHz	...	...	$<510$	$\lesssim 1.76 \times 10^{38}$
VLA	3 GHz	...	...	$340 \pm 30$	$(2.51 \pm 0.22) \times 10^{38}$
VLA	6 GHz	...	...	$221 \pm 21$	$(3.26 \pm 0.31) \times 10^{38}$
VLA	9 GHz	...	...	$150 \pm 10$	$(3.32 \pm 0.22) \times 10^{38}$

**Note.** Magnitudes  $m_\lambda$  are corrected for Galactic extinction,  $A_\lambda$ , in the direction of the burst (Fitzpatrick & Massa 2007). Data are from the Swift archive (Program 1619112), SDSS DR12 (Ahumada et al. 2020), Pan-STARRS DR1 (Chambers et al. 2016), 2MASS (Skrutskie et al. 2006), and AllWISE (Wright et al. 2010; Cutri et al. 2021; ). The uGMRT and VLA measurements are from Wharton et al. (2021b), Ricci et al. (2021), and Ravi et al. (2021). Upper limits correspond to the estimated  $3\sigma$  confidence.

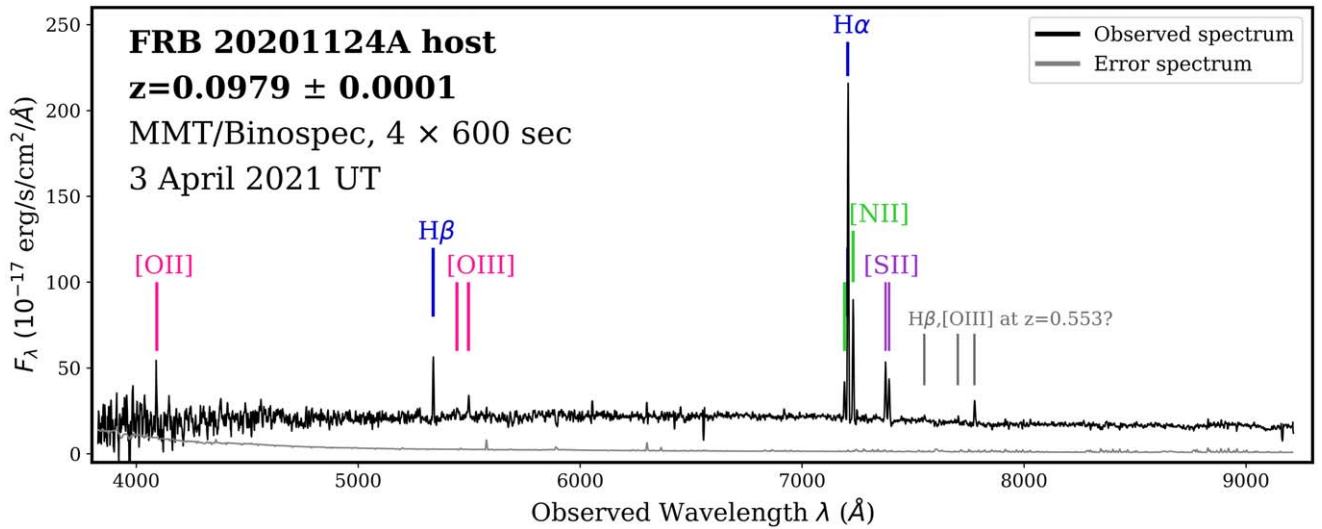
“inverse” prior in which brighter candidate hosts have higher prior probability according to their number density on the sky (Equations 4 and 12 in Aggarwal et al. 2021) and assume an underlying “exponential” distribution model for the offsets (Equation 14 in Aggarwal et al. 2021). We thus confidently assign SDSS J050803.48+260338.0 as the host galaxy of FRB 20201124A.

We initiated spectroscopic observations of the host of FRB 20201124A with the Binospec imaging spectrograph (Fabricant et al. 2019) mounted on the 6.5 m MMT Observatory atop Mount Hopkins, Arizona (Program UAO-G195-21A; PI: Fong) on 2021 April 3 UTC. The preliminary results of these observations were reported in Kilpatrick et al. (2021). We obtained  $4 \times 600$  s of exposures with the 270l grating and the LP3800 spectroscopic filter to mitigate the effects of second-order light contamination. The central wavelength was 6500 Å to cover a wavelength range of  $\sim 3800$ – $9200$  Å, and the 1'' slit was oriented at a position angle  $145^\circ$  East of North. We used the Python Spectroscopic Data Reduction Pipeline (PypeIt; Prochaska et al. 2020) for data processing on the overscan-subtracted images from the MMT archive. In PypeIt, we apply a flat-field correction and perform wavelength calibration and spectral extraction (using the `boxcar` method with a  $2''.4$  radius in order to include all of the extended line emission flux). We applied an absolute flux calibration using observations of the spectrophotometric standard Feige 34 taken on the same night. We coadded the 1D spectra and scaled the flux of the resulting coaddition to match the galaxy’s measured *r*-band magnitude. Finally, we applied a telluric correction using an atmospheric model. We corrected the spectrum for Galactic extinction using the Cardelli et al. (1989) extinction law and  $A_V = 2.024$  mag in the direction of the burst. The final 1D spectrum of the host of FRB 20201124A is displayed in Figure 3.

We detect several clear emission features: [O II] $\lambda 3727$ , H $\beta$  $\lambda 4861$ , [O III] $\lambda 5007$ , H $\alpha$  $\lambda 6563$ , [N II] $\lambda 6548$  and  $\lambda 6583$ , and [S II] $\lambda 6716$  and  $\lambda 6731$ . From these lines, we derive a common redshift of  $z = 0.0979 \pm 0.0001$ , consistent with the SDSS and PS1 photometric redshifts. At this redshift, the projected physical offset between the VLBI burst position and host center is  $1.29 \pm 0.05$  kpc. Using a value of  $\text{DM}_{\text{FRB}} \approx 414$   $\text{pc cm}^{-3}$ , the DM for the Galactic interstellar medium (ISM) in the direction of the FRB  $\text{DM}_{\text{ISM}} = 123$   $\text{pc cm}^{-3}$  (Cordes & Lazio 2002), and  $\text{DM}_{\text{MW, Halo}} = 50$   $\text{pc cm}^{-3}$  for the Milky Way halo (Prochaska & Zheng 2019) and assuming for the host  $\text{DM}_{\text{host}} = 50(1+z)$   $\text{pc cm}^{-3}$ , we find that the cosmic DM is  $\text{DM}_{\text{cosmic}} \approx 186$   $\text{pc cm}^{-3}$ . This derived value of  $\text{DM}_{\text{cosmic}}$  is in excess of the Macquart relation (which provides a relationship between  $\text{DM}_{\text{cosmic}}$  and  $z$ ; Macquart et al. 2020), which predicts  $\text{DM}_{\text{cosmic}} \approx 82$   $\text{pc cm}^{-3}$ . This can be reconciled if the DM intrinsic to the host or FRB environment is significantly larger than the value for  $\text{DM}_{\text{host}}$  assumed here, e.g.,  $\text{DM}_{\text{host}} = 100(1+z)$   $\text{pc cm}^{-3}$ .

We also remark on the presence of faint emission features redward of 7500 Å, with the strongest feature at 7777.78 Å (Figure 3). These features do not correspond to any known emission lines at  $z = 0.0979$ . Instead, we tentatively identify these features as H $\beta$  and [O III] $\lambda 4959$  and  $\lambda 5007$  from a *background* (likely unrelated; see below) galaxy at a common redshift of  $z = 0.5531$ .<sup>22</sup> The strongest of the features is visible in each of the individual exposures and has a spatial offset of  $\sim 2$  pixels from the host galaxy continuum in all frames. Using the known position angle of the slit, we determine that the emission originates from a source  $\sim 0''.5$  offset to the northwest of the host galaxy center in projection. This emission is not

<sup>22</sup> We note that given the high Galactic extinction and the low S/N with which we detect the redder emission features, the lack of detected [O II] at the same redshift is not surprising.



**Figure 3.** MMT/Binospec spectroscopy of the putative host galaxy of FRB 20201124A. The locations of several emission lines are marked, at a common redshift of  $z = 0.0979 \pm 0.0001$ . We also detect a few emission features redward of  $7500 \text{ \AA}$  (most prominently at  $7778 \text{ \AA}$ ), which we tentatively identify as  $H\beta$  and  $[O \text{ III}]$  emission from a background, spatially coincident but otherwise unrelated galaxy at  $z = 0.5531$ .

(The data used to create this figure are available.)

consistent with the VLBI position of the FRB, and is not readily visible in any of the available archival imaging. Adopting the Macquart relation and an estimate of its intrinsic scatter (parameterized with  $F = 0.3$ ; Macquart et al. 2020), the PDF for the cosmic DM  $P(\text{DM}_{\text{cosmic}}|z)$  yields a lower bound of  $\text{DM}_{\text{cosmic}}^{\text{min}} = 311 \text{ pc cm}^{-3}$  (95% confidence level for  $z = 0.55$ ). Combined with  $\text{DM}_{\text{ISM}} = 123 \text{ pc cm}^{-3}$  (Cordes & Lazio 2002), we recover  $\text{DM}_{\text{FRB}} > 434 \text{ pc cm}^{-3}$ , which exceeds the measured value even before including the Galactic halo or any host DM contribution. Therefore, we conclude this putative galaxy is not the host of FRB 20201124A.

### 2.3. Swift/XRT Observations

The X-ray Telescope (XRT) on board the Neil Gehrels Swift Observatory (Swift; Gehrels et al. 2004) observed the location of FRB 20201124A in a series of two observations: ObsID 00014258001, starting on 2021 April 6 at 19:48:08 UTC, and ObsID 00014258002, starting on 2021 April 7 at 06:30:37 UTC, under Program 1619112 (PI: L. Piro) for 4.92 ks each. Previous analyses of parts of these data yielded X-ray luminosity upper limits of  $L_X \lesssim 2.2\text{--}4.4 \times 10^{42} \text{ erg s}^{-1}$  (reported in Campana 2021 and O’Connor et al. 2021).

We retrieve the aforementioned Swift/XRT data from the HEASARC archive. We produce new event files for both observations using the `xrtpipeline` tool (HEASoft software, v.6.26; Blackburn et al. 1999; NASA High Energy Astrophysics Science Archive Research Center (HEASARC), 2014) and `caldb` files (v.20200724). We stack the observations utilizing the `XSELECT` tool and obtain a total exposure time of 9.83 ks. Within a source aperture of  $20''$  in radius centered on the optical host centroid, we detect two counts in the 0.3–10.0 keV range. Using the Poisson single-sided upper limits introduced in Gehrels (1986), we calculate a  $3\sigma$  upper limit of  $<1.11 \times 10^{-3} \text{ cts s}^{-1}$ . To convert to flux, we employ the standard relation from Watson (2011) between  $A_V$  and  $N_{\text{H,int}}$ , the hydrogen column density intrinsic to the host galaxy, using  $A_V = 1.5 \text{ mag}$  (Section 3.3) to obtain

$N_{\text{H,int}} = 3.3 \times 10^{21} \text{ cm}^{-2}$ . We also assume a standard power-law spectrum with a photon index  $\Gamma_X = 2$  (for consistency with Campana 2021, O’Connor et al. 2021, and other synchrotron sources; Ishibashi & Courvoisier 2010) and the Galactic contribution to the hydrogen column density in the direction of the FRB,  $N_{\text{H,MW}} = 4.49 \times 10^{21} \text{ cm}^{-2}$  (Willingale et al. 2013) to calculate the unabsorbed X-ray flux to be  $F_X \lesssim 1.09 \times 10^{-13} \text{ erg s}^{-1} \text{ cm}^{-2}$  (0.3–10.0 keV). This translates to a  $3\sigma$  upper limit on the X-ray luminosity of  $\nu L_X \lesssim 1.3 \times 10^{42} \text{ erg s}^{-1}$  at a central energy of 1.7 keV (Table 2). This result is in agreement with the previous analyses reported in Campana (2021) and O’Connor et al. (2021).

## 3. The Host Galaxy Properties of FRB 20201124A

### 3.1. Optical and Near-infrared Properties: A Dusty, Star-forming Galaxy

Here, we explore the colors and emission line diagnostics of the host of FRB 20201124A in the context of the degree of global star formation. We first remark on the degree of contribution of the  $z = 0.553$  background galaxy to the existing host photometry in Table 2. If we assume that the background galaxy has a luminosity of  $L^*$ , this corresponds to an apparent brightness of  $r \approx 21.5 \text{ mag}$ , calculated from the galaxy luminosity function in the appropriate rest-frame band (Willmer et al. 2006). Given the foreground host galaxy brightness of  $r \approx 17.87 \text{ mag}$ , the background galaxy would contribute only 3% to the total flux, or 0.04 mag. Thus, we do not expect any background galaxy to contribute significantly to the flux and affect our subsequent conclusions.

At the most basic level, we first compare the colors of the host of FRB 20201124A to characterize its nature in the context of other galaxies. The rest-frame  $U-V$  and  $V-J$  colors are often used to separate star-forming (SF) from quiescent galaxies on a  $UVJ$  diagram (Williams et al. 2009). For the host of FRB 20201124A at  $z = 0.0979$ , the rest-frame  $U-V$  and  $V-J$  colors roughly correspond to  $u-g \approx 1.6 \text{ mag}$  and

**Table 3**  
FRB 20201124A Host Nebular Emission Line Fluxes

Line	$F_\lambda$ ( $10^{-15}$ erg s $^{-1}$ cm $^{-2}$ )
H $\beta$	$1.23^{+0.30}_{-0.23}$
[O III] $\lambda$ 4959	$0.12^{+0.07}_{-0.03}$
[O III] $\lambda$ 5007	$0.38^{+0.21}_{-0.11}$
[N II] $\lambda$ 6548	$0.85^{+0.20}_{-0.16}$
H $\alpha$	$5.69^{+1.49}_{-0.99}$
[N II] $\lambda$ 6583	$2.53^{+0.60}_{-0.47}$
[S II] $\lambda$ 6716	$1.08^{+0.25}_{-0.20}$
[S II] $\lambda$ 6731	$0.84^{+0.19}_{-0.15}$

**Note.** These values are derived from `Prospector` and are corrected for underlying stellar absorption and Galactic extinction in the direction of the host.

$g - J \approx 1.4$  mag. In the context of the  $UVJ$  diagram, the host of FRB 20201124A exhibits redder  $U - V$  colors than unobscured SF galaxies but is consistent with the colors of dusty SF galaxies (Fumagalli et al. 2014; Fang et al. 2018). Turning to the infrared, WISE colors may also be used to distinguish various star-forming galaxy types (e.g., normal star-forming, luminous infrared galaxies (LIRGs), and starbursts) from those that host quasars or obscured AGN (Wright et al. 2010). Using the extinction-corrected WISE colors (in the native Vega magnitude system), we find  $W1 - W2 \approx 0.31$  mag and  $W2 - W3 \approx 4.17$  mag. This corresponds to the parameter space occupied by LIRGs and starburst galaxies (Wright et al. 2010). Based on the WISE colors, we also note that the galaxy is unlikely to host a strong active galactic nucleus (AGN), since the majority of such hosts have red ( $W1 - W2 > 0.6$  mag) colors (Wu et al. 2012).

We additionally explore the location of the host of FRB 20201124A on the Baldwin–Phillips–Terlevich (BPT) diagram (Baldwin et al. 1981), which distinguishes SF galaxies from low-ionization nuclear emission-line region (LINER) galaxies and those that host AGN according to their ratios of line fluxes,  $\log([\text{N II}]\lambda 6583/\text{H}\alpha)$  and  $\log([\text{O III}]\lambda 5007/\text{H}\beta)$ . To determine the line fluxes,  $F_\lambda$ , we use the `Prospector` code (see Section 3.3 of Leja et al. 2017; Johnson et al. 2021) to fit a Gaussian line spread function with variable amplitude, width, and a small perturbation allowed around the measured line center for each generated model spectrum. This Gaussian sits on top of the model stellar spectrum, naturally including the effect of the underlying stellar absorption. Formally, the amplitude of the Gaussian is a compromise between the expectation value based on the CLOUDY photoionization model built into `Python-fsps` (Flexible Stellar Population Synthesis; Conroy et al. 2009; Conroy & Gunn 2010) and the observed spectrum (see Appendix E of Johnson et al. 2021); in practice, for the strong lines measured in this spectrum, the likelihood is dominated by the data, and the reported luminosities represent the observed luminosities corrected for the underlying stellar absorption. We report the line fluxes in Table 3. These line fluxes yield ratios of  $\log([\text{N II}]\lambda 6583/\text{H}\alpha) = -0.35$  and  $\log([\text{O III}]\lambda 5007/\text{H}\beta) = -0.51$ . Compared to the BPT relations, this places the host of FRB 20201124A in the region occupied by SF galaxies (Brinchmann et al. 2008). Based on an initial sample of eight FRB hosts, Heintz et al. (2020) found that they overall exhibit harder ionization fields

than expected from the normal galaxy population, pointing toward a preference for LINER or AGN origins. By contrast, the emission line flux ratios and optical/infrared (IR) colors classify the host of FRB 20201124A as a dusty SF galaxy with no clear sign of AGN or LINER emission.

### 3.2. Nebular Emission: Star Formation Rate and Metallicity

Given the SF designation of the galaxy, we use the observed H $\alpha$  line flux to obtain the host global star formation rate (SFR). We correct the line emission for stellar absorption and correct the H $\alpha$  line flux for the Balmer absorption (from stellar population modeling; Section 3.3),  $F_\lambda(\text{H}\alpha)/F_\lambda(\text{H}\beta) \approx 6.6$ , which is significant compared to the theoretical value for Case B recombination in the absence of dust extinction of  $\sim 2.86$  (Osterbrock & Ferland 1989). Applying the Calzetti et al. (2000) extinction law for actively star-forming galaxies yields a dust extinction of  $A_V = 1.66 \pm 0.33$  mag and  $A(\text{H}\alpha) = 1.37 \pm 0.33$  mag. We calculate a dust-corrected line luminosity of  $L(\text{H}\alpha) = 4.95^{+1.30}_{-0.86} \times 10^{42}$  erg s $^{-1}$  yielding  $\text{SFR} = 2.12^{+0.69}_{-0.28} M_\odot \text{ yr}^{-1}$  (Kennicutt 1998; Moustakas et al. 2006), assuming a Chabrier initial mass function (IMF; Chabrier 2003).

We infer the gas-phase metallicity of the host galaxy based on the strong-line diagnostics ratio,  $\text{O3N2}^{23}$  of Hirschauer et al. (2018), which yields an oxygen abundance of  $12 + \log(\text{O}/\text{H}) = 9.03^{+0.15}_{-0.24}$ . We chose this calibration as it minimizes the effects of dust obscuration on the individual line fluxes while including the large set of available lines detected in the spectrum. Relative to the stellar mass of the galaxy (see Section 3.3), the oxygen abundance is consistent with the mass–metallicity relation of SF galaxies at similar redshifts (Maiolino et al. 2008).

### 3.3. Stellar Population Modeling

We determine the stellar population properties of the host galaxy of FRB 20201124A with `Prospector`, a Python-based stellar population inference code (Leja et al. 2017; Johnson et al. 2021). We jointly fit the observed photometry and spectroscopy using the nested sampling routine, `dynesty` (Speagle 2020), and build the model spectral energy distribution (SED) with `Python-fsps` (Conroy et al. 2009; Conroy & Gunn 2010). Our precise modeling assumptions and parameter definitions are described in the Appendix, and the priors on these properties are listed in Table A1.

We jointly fit the observed photometry and spectrum of the host of FRB 20201124A, both corrected for Milky Way extinction and weighted by the  $1\sigma$  photometric uncertainties and error spectrum. We run multiple fits, employing a delayed- $\tau$  parametric SFH, and a nonparametric SFH. While the use of nonparametric SFHs has been demonstrated to represent a more physically realistic representation of galaxy histories (Conroy 2013; Leja et al. 2019), such models are not yet broadly used in transient host galaxy literature. The choice of SFH also can result in known offsets of stellar population properties (see Leja et al. 2019). Thus, including the derived properties of the parametric SFH fit here enables a direct comparison to other FRB hosts that have been modeled with similar assumptions and to the `Prospector` parametric SFH fitting results of Ravi et al. (2021) and Piro et al. (2021).

<sup>23</sup>  $\text{O3N2} = \log([\text{O III}]\lambda 5007/\text{H}\beta)/([\text{N II}]\lambda 6583/\text{H}\alpha)$ .

**Table 4**  
Derived Host Galaxy Properties of FRB 20201124A

Property	Value	Units
$z$	$0.0979 \pm 0.0001$	
R.A. (J2000)	$5^{\text{h}}08^{\text{m}}03^{\text{s}}.477$	
decl. (J2000)	$+26^{\circ}03'37''.93$	
$\delta R$ (VLBI)	$0.71 \pm 0.03$	"
$\delta R$ (VLBI)	$1.29 \pm 0.05$	kpc
SFR ( $H\alpha$ )	$2.1^{+0.7}_{-0.3}$	$M_{\odot} \text{ yr}^{-1}$
SFR (3–1100 $\mu\text{m}$ )	$4.0^{+0.9}_{-0.5}$	$M_{\odot} \text{ yr}^{-1}$
SFR (radio) <sup>a</sup>	2.2–5.9	$M_{\odot} \text{ yr}^{-1}$
$12+\log(\text{O}/\text{H})$	$9.03^{+0.15}_{-0.24}$	
$\log(L_B/L_{\odot})$	10.10	
Prospector Parametric Fit		
$\log(M_*/M_{\odot})$	$10.23^{+0.02}_{-0.03}$	
$t_m$	$4.97^{+0.36}_{-0.52}$	Gyr
$t_{\text{max}}$	$11.00^{+0.92}_{-1.35}$	Gyr
$\tau$	$5.62^{+0.86}_{-1.02}$	Gyr
$\log(Z_*/Z_{\odot})$	$-0.87 \pm 0.06$	
$\log(Z_{\text{gas}}/Z_{\odot})$	$0.13 \pm 0.01$	
$A_{V,\text{old}}$	$1.02 \pm 0.04$	mag
$\text{SFR}_{\text{SED}}$	$2.43 \pm 0.13$	$M_{\odot} \text{ yr}^{-1}$
Prospector Nonparametric Fit		
$\log(M_*/M_{\odot})$	$10.28 \pm 0.05$	
$t_m$	$6.16^{+0.75}_{-0.80}$	Gyr
$\log(Z_*/Z_{\odot})$	$-0.58 \pm 0.22$	
$\log(Z_{\text{gas}}/Z_{\odot})$	$0.17^{+0.29}_{-0.19}$	
$A_{V,\text{young}}$	$0.91^{+0.44}_{-0.39}$	mag
$A_{V,\text{old}}$	$0.81^{+0.20}_{-0.16}$	mag
$\text{SFR}_{\text{SED}}^{\text{b}}$	$1.50^{+0.52}_{-0.35}$	$M_{\odot} \text{ yr}^{-1}$
sSFR(100 Myr)	$1.38^{+0.75}_{-0.49}$	$10^{-10} \text{ yr}^{-1}$

**Notes.** Properties of FRB 20201124A and its host galaxy determined in this work. The `Prospector` parametric fit is characterized by a Milky Way extinction law and delayed- $\tau$  SFH. Quoted upper limits correspond to the 99.7% quantile. The `Prospector` property definitions are described in Section 3.3

<sup>a</sup> Range set by frequency and calibration method (Yun & Carilli 2002; Murphy et al. 2011).

<sup>b</sup> Corresponds to ongoing SFR in the most recent age bin.

The results of the parametric SFH and nonparametric SFH fits are listed in Table 4. In particular, we report the median values and bounds corresponding to 68% credible intervals. The model representing the median of the nonparametric SFH posterior is plotted along with the observed photometry and spectroscopy in Figure 4. In terms of stellar mass, dust content, and low stellar metallicity, we find similar values between our parametric and nonparametric SFH fits (Table 4). We further find a somewhat older median mass-weighted age of  $t_m \approx 6.2$  Gyr in our nonparametric SFH fit. Comparing our parametric SFH results to the modeling results of Ravi et al. (2021) and Piro et al. (2021), our results are broadly consistent, although we report a mass-weighted age that is a bit older than implied by their fits.

Next, we investigate the cause of the low stellar metallicity. First, we remove the W3 and W4 fluxes from our fits, but still recover the same preference for a low stellar metallicity. Next, we fix the stellar metallicity to the solar value and re-run the fit. This reveals that the continuum S/N in the spectroscopy is too

low to put strong constraints on the metallicity. The low stellar metallicity is instead largely driven by the relatively blue near-IR colors (specifically the WISE W1–W2 color). `Prospector` is able to provide an adequate fit to the photometry assuming solar metallicity by dramatically lowering the emission from polycyclic aromatic hydrocarbon (PAH) molecules, thereby removing the strong 3.3  $\mu\text{m}$  PAH emission line. However, to explain the W3 and W4 fluxes without PAH emission would require an extraordinarily bright IR AGN with  $\sim 58$  times the bolometric luminosity of the galaxy. We are unable to distinguish between the following three scenarios without more data: (a) the stellar metallicity is truly as low as measured, (b) there is an extremely bright IR AGN that has also destroyed all of the PAH molecules, or (c) the 3.3  $\mu\text{m}$  PAH emission line alone is much dimmer in this galaxy than in galaxies with comparable amounts of PAH content. We note that removing the W3 and W4 fluxes entirely removes the need for a bright IR AGN.

### 3.4. Star Formation and Mass Assembly Histories

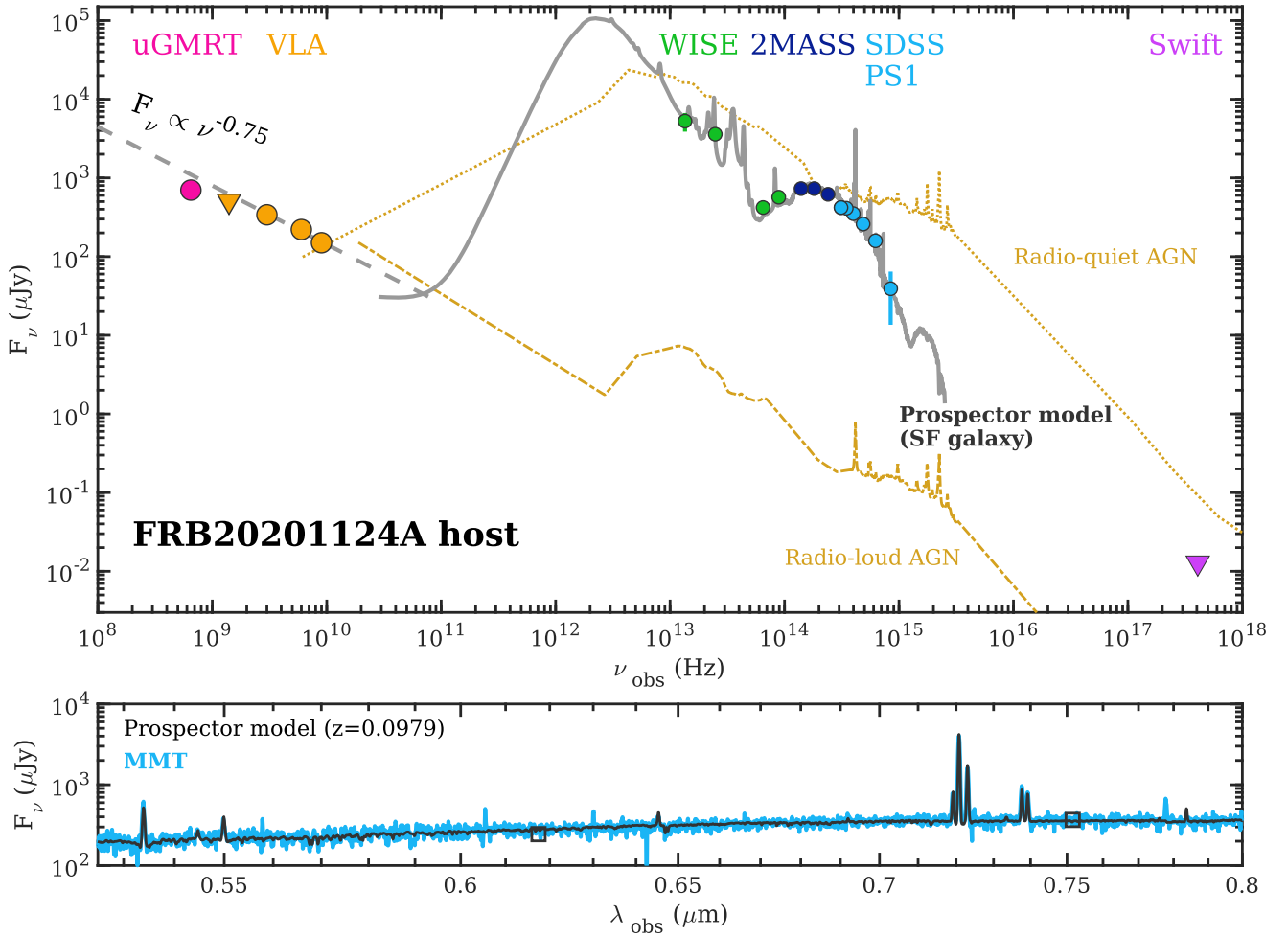
Using the results of the nonparametric SFH modeling, we are able to construct the star formation and mass assembly histories. The SFR as a function of lookback time (where  $t_{\text{lookback}}$  is defined in the frame of the FRB host) is displayed in Figure 5. We find that the SFR was roughly constant for most of the galaxy’s history, at a rate of  $\sim 2$  times the present-day value, before decreasing to  $\sim 1.5 M_{\odot} \text{ yr}^{-1}$  at  $t_{\text{lookback}} \approx 30$  Myr.

We also construct the cumulative mass assembly history of the host by calculating the fraction of mass using  $N = 500$  posterior samples of  $M(t)$ ; (i.e., the current mass in stars and stellar remnants as a function of creation time) from the `Prospector` nonparametric fit.<sup>24</sup> For each posterior sample, the cumulative  $M'(t)$  is constructed, and then this vector is divided by the total mass formed in that posterior sample. The reported values are the posterior median cumulative  $M'(t)$  formed in each bin, and the uncertainties are taken as the 16% and 84% values of the posterior. The result is shown in Figure 5. A large majority of the stellar mass,  $\sim 91.4\%$ , was formed by  $t_{\text{lookback}} = 1$  Gyr. By  $t_{\text{lookback}} = 100$  Myr, 99.1% of the host mass was formed by this time. Thus, despite the slight increase in the median absolute SFR at  $t_{\text{lookback}} \approx 30$ –300 Myr, the peak was not prolonged or pronounced enough to contribute significantly to the total mass budget of the galaxy. In fact, within the 68% confidence interval, the SFH is fairly constant until  $t_{\text{lookback}} \approx 30$  Myr.

We further find evidence for a hot dust emission component with  $f_{\text{AGN}} \approx 0.04$ , corresponding to a mid-IR luminosity contribution of a potential AGN to the total mid-IR galaxy luminosity of  $\sim 20\%$ . This model parameter is typically interpreted as dust emission heated by a central AGN. However, we caution that there are other potential origins of dust heated to high temperatures, including extreme star formation (Leja et al. 2018), or higher centralized stellar densities (Groves et al. 2012). Thus, while we cannot rule out the presence of an AGN completely, other multiwavelength AGN diagnostics do not support an AGN as a strong contributor to the host of the FRB 20201124A.

<sup>24</sup> A sample-by-sample approach is necessary due to the strong bin-to-bin correlation in the mass formed in each time bin.





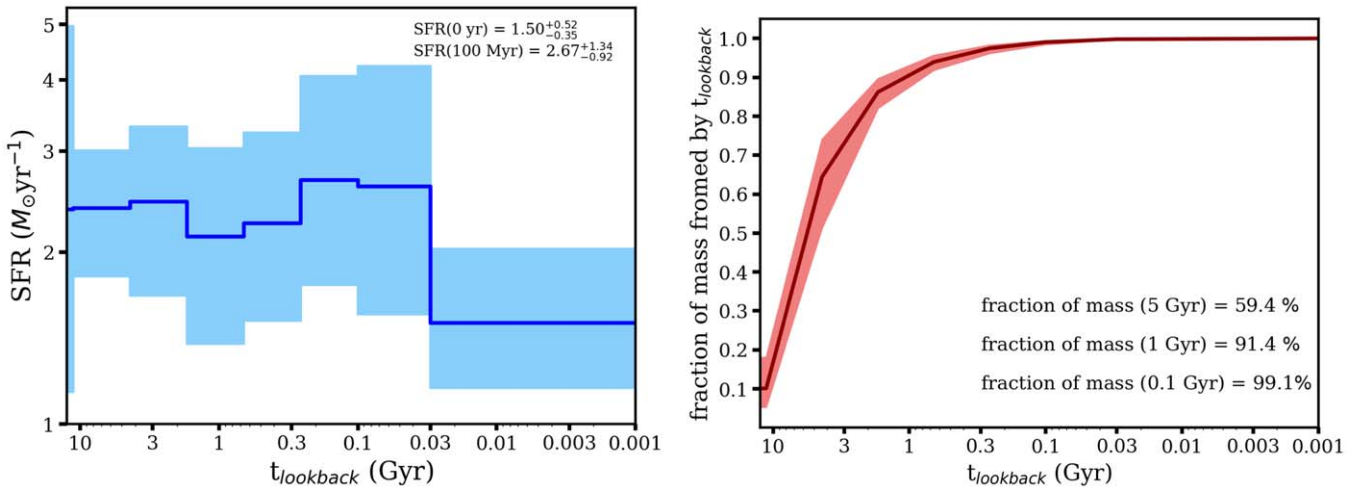
**Figure 4.** Top: broadband SED of the host galaxy of FRB 20201124A with data taken from uGMRT (Wharton et al. 2021b), VLA (Ricci et al. 2021; Ravi et al. 2021), WISE, 2MASS, PS1, SDSS, and Swift/XRT (Campana 2021; O’Connor et al. 2021 and re-analyzed in this work). Circles denote detections and triangles denote  $3\sigma$  upper limits. Also shown are the star-forming galaxy model from *Prospector* (gray line) and the best-fit power law to the radio data at  $3\text{ GHz} \lesssim \nu \lesssim 9\text{ GHz}$ , representing a synchrotron component ( $F_\nu \propto \nu^{-0.75}$ ; dashed line). The normal star-forming model provides a good fit to the data, whereas the radio-quiet and radio-loud AGN templates (tan dotted and dashed-dotted lines; Shang et al. 2011), scaled to the radio fluxes, do not provide adequate matches to the broadband data. Bottom: MMT spectrum (blue) vs. wavelength, corrected for Galactic extinction, with the *Prospector* model spectrum and photometry (black lines and squares) at  $z = 0.0979$ , demonstrating the agreement of the continuum shape and nebular emission lines.

### 3.5. Physical Origin of the Persistent Radio Emission

We now address the origin of the persistent radio emission reported by uGMRT and the VLA (Wharton et al. 2021b; Ricci et al. 2021). The lack of a counterpart in the milliarcsecond resolution 1.374 GHz VLBI observations (Marcote et al. 2021; Ravi et al. 2021), together with the fact that the persistent emission is unresolved to the VLA at 6 GHz with a beam size of  $\sim 11''$  and an  $S/N \approx 15$  (Ravi et al. 2021), constrains its size to the range  $0.2\text{--}3''$  (or  $\sim 0.4\text{--}5.5\text{ kpc}$  at  $z = 0.0979$ ; see Section 2.2). As it pertains to FRBs, there are three primary sources of persistent radio emission to consider: a compact radio source akin to that detected in association with FRB 20121102A (Chatterjee et al. 2017), emission driven by disks, winds, or jets from an AGN (Panessa et al. 2019), or star formation in the galaxy (Condon 1992). The nondetection of persistent radio emission in high-resolution VLBI observations (Marcote et al. 2021) immediately rules out a compact source (associated with either plerion-type emission like that seen in FRB 20121102A or a core-dominated AGN) and instead points to an origin from a more extended spatial scale. The source is detected at 650 MHz (uGMRT; Wharton et al. 2021b), 3 GHz,

6 GHz, and 9 GHz (VLA; Ravi et al. 2021; Ricci et al. 2021), while there is an upper limit on the 1.4 GHz emission (Ravi et al. 2021). Emission was also reported at 22 GHz, although this emission is potentially collocated with the FRB position (Piro et al. 2021). The reported 650 MHz to 9 GHz fluxes, luminosities, and upper limits from these sources are compiled in Table 2. The luminosity of the source is  $\nu L_\nu \approx (2.5\text{--}3.3) \times 10^{38}\text{ erg s}^{-1}$ . Although the centroids of the reported uGMRT and VLA persistent radio emission are offset from each other, they are formally consistent within their quoted uncertainties (Figure 2). Thus, in what follows, we are treating the uGMRT and VLA emission as if they are originating from the same physical process, and the same general source.

We use  $\chi^2$ -minimization to fit power-law models to the data ( $F_\nu \propto \nu^\beta$ ), incorporating the  $1\sigma$  uncertainties on the fluxes. We find  $\beta_{650\text{MHz}\rightarrow 3\text{GHz}} = -0.47 \pm 0.11$ , with a steepening to  $\beta_{3\text{GHz}\rightarrow 9\text{GHz}} = -0.75 \pm 0.13$ . Fitting a broken power-law model to all four data points, using the break frequency and smoothness as additional free parameters, we find it is only possible to constrain the location of the steepening to  $\sim 4.7\text{--}7.6\text{ GHz}$  with the available data, with the unconstrained



**Figure 5.** Left: derived SFR vs. lookback time ( $t_{\text{lookback}}$ ) of the host of FRB 20201124A for each of the eight time bins. The blue line represents the median, and the shaded region represents the 68% quantile of each bin. The SFR was fairly constant for most of the host’s history, with a notable absence of any starburst. Right: mass assembly history vs. lookback time of the host of FRB 20201124A (where  $t_{\text{lookback}} = 0$  corresponds to the redshift of the host). The shaded region represents the 68% quantile. By  $t_{\text{lookback}} = 1$  Gyr (100 Myr),  $\sim 91.4\%$  ( $\sim 99.1\%$ ) of the galaxy’s total mass was already formed. The history implies longer delay times for progenitors that trace stellar mass.

smoothness of the break driving the uncertainty. This is in good agreement with the results from Ravi et al. (2021). As the PRS is reported to be unresolved in the low angular resolution VLA and GMRT observations, there is no need to account for the impact of a changing beam size on the flux density obtained from these observations.

We next consider an AGN origin for the radio emission, as the reported locations of the persistent emission are also formally consistent with the host centroid (Figure 2). The nondetection of X-ray emission with Swift/XRT to an unabsorbed flux of  $F_X \lesssim 1.1 \times 10^{-13} \text{ erg s}^{-1} \text{ cm}^{-2}$  (0.3–10 keV; Section 2.3), or  $\nu L_\nu \lesssim 1.3 \times 10^{42} \text{ erg s}^{-1}$ , constrains  $\log_{10}(L_R/L_X) \gtrsim -3.5$ , placing any potential AGN in the “radio-loud” category (Terashima & Wilson 2003). To demonstrate this, we adopt a radio-quiet AGN broadband SED template (Shang et al. 2011) and scale the model to the radio fluxes. Figure 4 demonstrates that this model both violates the X-ray upper limit and also overpredicts the IR and optical fluxes. However, the  $\log_{10}(L_R/L_X)$  ratio is consistent with a radio-loud AGN, but a similarly scaled template (Shang et al. 2011) underestimates the optical/IR fluxes by three orders of magnitude (as these generally are prone to significant obscuration; Figure 4). We further calculate the total IR luminosity ( $L_{\text{TIR}}$ ; 3–1100  $\mu\text{m}$ ) from the `Prospector` model and find  $\log(L_{\text{TIR}}/L_\odot) = 10.4^{+0.09}_{-0.06}$ , which follows the canonical radio–TIR relations assuming pure star formation (Molnár et al. 2021). Thus, in support of the conclusions drawn from the emission line analysis, we consider it unlikely that an AGN is a dominant source of the observed persistent radio emission.

Finally, we consider whether the radio emission originates from recent star formation. Radio emission from galaxies is a combination of nonthermal, synchrotron emission from relativistic electrons accelerated by supernovae, with a canonical spectral index  $\beta \approx -0.75$ , and thermal, free–free emission with a flatter spectral index  $\beta \approx -0.1$  (Condon 1992). At the frequencies observed for the FRB host (650 MHz to 9 GHz), the synchrotron component is expected to dominate, while there is an observed flattening at  $\nu < 1$  GHz.

Given the constraints on the size of the emission region ( $\sim 0.2\text{--}3''$  based on the nondetection on VLBI scales and it

being unresolved with the VLA) and the fact that it is coincident with the nucleus of the galaxy, the PRS could be explained by diffuse circumnuclear emission, similar to the radio emission observed at the center of the Milky Way (Heywood et al. 2019) and other spiral galaxies (Ekers 1974; Condon 1980). Here, the radio emission is produced by a mixture of diffuse high-energy electrons accelerated by a combination of supernovae (SNe), supernova remnants, ionized thermal emission, and highly magnetized filaments (Yusef-Zadeh et al. 2004), all correlated with recent star formation in the galactic center. In this scenario, the spectral flattening observed below 5 GHz can also be attributed to free–free absorption by thermal emission embedded in this central region. In general, the radio emission could potentially be connected to the evidence of a hotter dust component from the optical and IR SED. We also note that Piro et al. (2021) suggests from high-frequency observations that the radio emission is colocated with the position of the FRB, although further high-resolution observations of the host are needed to precisely locate the region or regions of emission.

Using standard relations relating the radio continuum luminosity to the SFR, we derive  $\text{SFR} \approx 2.2\text{--}5.9 M_\odot \text{ yr}^{-1}$  (Yun & Carilli 2002; Murphy et al. 2011), with the range depending on the SFR calibration used. From the total IR luminosity, we similarly derive  $\text{SFR} \approx 4.00^{+0.93}_{-0.51} M_\odot \text{ yr}^{-1}$  (Hao et al. 2011). These derived values are slightly larger than the dust-corrected value inferred from the  $\text{H}\alpha$  line emission.<sup>25</sup> Given this consistency, we consider recent star formation to be the dominant, if not the sole contributor to the observed persistent radio emission in the host of FRB 20201124A.

<sup>25</sup> We note that the small differences in derived SFR can be attributed to a number of factors, including incomplete dust correction, contributions to the TIR luminosity by the heating of dust, or the fact that the  $\text{H}\alpha$ –SFR conversion is systematically uncertain at the level of a factor of two (see Theios et al. 2019).

#### 4. The Host Properties of FRB 20201124A in Context: Implications for the Progenitor

FRB 20201124A now joins the small population of known repeating FRBs with identified hosts: FRB 20121102A (Chatterjee et al. 2017; Tendulkar et al. 2017), FRB 20180916B (Marcote et al. 2020), FRB 20190711A (Heintz et al. 2020; Macquart et al. 2020), FRB 20200120E (Bhardwaj et al. 2021a), FRB 190520 (Li et al. 2021), and FRB 20181030A (Bhardwaj et al. 2021b). An additional source of FRB-like emission, FRB 200428, was traced back to a magnetar in our Galaxy (CHIME/FRB Collaboration et al. 2020). Like the host of FRB 20201124A, all of these galaxies are actively forming stars at low to moderate rates of  $\sim 0.06\text{--}2 M_{\odot} \text{ yr}^{-1}$  (Gordon et al. 2004; Heintz et al. 2020; Li et al. 2021); the inferred SFR for the host of FRB 20201124A is at the upper end of this range. The FRB 20201124A host is the most massive when compared to the cosmological hosts beyond 5 Mpc (Heintz et al. 2020) but is less massive than the Milky Way (McMillan 2011; Licquia & Newman 2015) and M81 (de Blok et al. 2008), consistent with the stellar mass evolution of normal star-forming galaxies to low redshifts. Thus, in terms of specific SFR (i.e., SFR per unit stellar mass), the host of FRB 20201124A is unremarkable compared to the host galaxies of other repeating FRBs, which span a wide range of  $\sim (0.1\text{--}11) \times 10^{-10} \text{ yr}^{-1}$ .

However, notable properties of the host in terms of the repeating FRB host population include its significant dust attenuation and potentially unusually low stellar metallicity of  $\sim (0.1\text{--}0.3)Z_{\odot}$  (although we note that the gas-phase metallicity is higher at  $\sim Z_{\odot}$ ). In terms of their emission line ratios, five other FRB hosts, including that of one other repeater (FRB 20121102A), lie in the general plane of SF galaxies (Heintz et al. 2020). Beyond FRB 20201124A, only FRBs 20191001 and 20190608 have hosts with faint radio emission interpreted as star formation (Bhandari et al. 2020b, 2020a).<sup>26</sup> However, unlike FRB 20201124A, all of these FRBs are apparent nonrepeaters.

At a projected physical offset of  $\sim 1.3$  kpc, FRB 20201124A is also more proximal to its host center than most FRBs with known hosts, in the lower  $\sim 10\%$  of the offset distribution (Heintz et al. 2020; Mannings et al. 2021). From the available data, the FRB position does not appear to be coincident with any flux enhancements, such as a spiral arm, as has been seen for some of the other FRBs (Mannings et al. 2021). However, higher-resolution imaging is needed to assess the presence of any underlying substructure.

Compared to the general galaxy population, the host of FRB 20201124A follows the standard relations for normal, star-forming galaxies at  $z \sim 0.1$ . The host lies on the star-forming main sequence of galaxies (Whitaker et al. 2012), demonstrating that it is forming stars at a similar rate to other galaxies of the same stellar mass. Its gas-phase metallicity and stellar mass also follow the mass–metallicity relation (Tremonti et al. 2004; Maiolino et al. 2008). While the host of FRB 20201124A exhibits significant dust content, this is not necessarily unexpected for star-forming galaxies in its mass range (Whitaker et al. 2012). The host SED additionally supports a hot dust component contributing at the level of 20% to the mid-IR luminosity, which cannot easily be attributed to a

strong AGN given the broadband data. However, the dust heating could be the result of higher stellar densities (as seen in M31; Groves et al. 2012; Viaene et al. 2017), and potentially related to the persistent radio emission on  $\lesssim 5$  kpc size scales, which we conclude to be due to recent circumnuclear star formation.

The properties and history of FRB 20201124A’s stellar population provide direct points of comparison to expectations for various progenitors. We first consider the production of (millisecond) magnetars through “ultra-prompt” channels, such as Type I superluminous SNe (SLSNe) or long-duration gamma-ray bursts (LGRBs; e.g., Metzger et al. 2015, 2017; Eftekhari et al. 2019). Such magnetars may naturally acquire their magnetic fields from their parent stars or via a convective dynamo shortly after collapse (e.g., Duncan & Thompson 1992; Raynaud et al. 2020). The existence of the persistent radio source coincident with FRB 20121102A (Chatterjee et al. 2017) has been interpreted as emission from a young magnetar nebula or low-luminosity AGN (Kashiyama & Murase 2017; Metzger et al. 2017; Margalit & Metzger 2018; Michilli et al. 2018; Eftekhari et al. 2019). The FRB source is also located in a star-forming knot in its dwarf host galaxy, similar to the properties of LGRBs and Type I SLSNe (Bassa et al. 2017; Tendulkar et al. 2017); taken together, these properties make ultra-prompt channels a compelling progenitor scenario to consider for repeating FRBs.

However, the hosts of LGRBs and SLSNe have median stellar masses and luminosities an order of magnitude lower than that of the host of FRB 20201124A (Savaglio et al. 2009; Vergani et al. 2015; Perley et al. 2016; Schulze et al. 2021); indeed it is rare for a SLSN or LGRB host to have an inferred stellar mass of  $>10^{10} M_{\odot}$  when considering similar redshifts. In addition, unlike what is observed in the host of FRB 20201124A, the host galaxies of LGRBs and SLSNe each exhibit a strong connection with enhanced global and local star formation, or starburst activity (Levesque et al. 2010; Lunnan et al. 2014; Perley et al. 2015; Hatsukade et al. 2018). By contrast, FRB 20201124A host’s star formation rate is remarkably constant over its  $>10$  Gyr history, with a recent decrease only in the last  $\sim 30$  Myr by a modest factor of  $\sim 2$ . In the context of an ultra-prompt progenitor channel, we do not find clear evidence of any past or recent starburst activity that could be connected to the birth of a very young ( $\lesssim$  few Myr) progenitor.

Thus, the host properties of FRB 20201124A, together with the lack of a compact radio remnant, contribute to the growing body of circumstantial evidence that such “ultra-prompt” channels are not dominant in the production of observed FRBs, and even repeating FRBs (Bhandari et al. 2020a; Heintz et al. 2020; Li & Zhang 2020; Safarzadeh et al. 2020). That said, as a fairly typical star-forming galaxy, the host of FRB 20201124A has properties that are consistent with those of core-collapse SNe (CCSNe; e.g., Kelly & Kirshner 2012; Galbany et al. 2016; Schulze et al. 2021). Magnetars produced in such “prompt” channels have been argued to be a dominant channel for the extragalactic population of FRBs (e.g., Bochenek et al. 2021; see also Chrimes et al. 2021). The delay times of CCSNe range from  $\sim$  few to 200 Myr, with a median of  $\sim 22$  Myr (Zapartas et al. 2017; Castrillo et al. 2021), which could be accommodated given the fairly constant host SFH.

<sup>26</sup> We note that the candidate host of FRB 20171020A also has faint radio SF, but its host association is less secure Mahony et al. (2018).

Given the moderate mass-weighted stellar population age of  $\sim 5\text{--}6$  Gyr, the host of FRB 20201124A can also accommodate progenitors that have longer delay times. Such “delayed” channels include the production of magnetars from compact object-related systems, including neutron star mergers, or the accretion-induced collapse (AIC) of a white dwarf (WD) to a neutron star (NS; Margalit et al. 2019). Such systems could have easily been formed earlier in the history of the host of FRB 20201124A, only to produce a magnetar (and resulting observable FRB activity) fairly recently. Further still, dynamical formation channels of compact object systems in globular clusters can have long delay times due to the presence of binaries or black holes, which inhibits mass segregation and interactions (Kremer et al. 2020). This was proposed as one of the explanations for the extremely old  $\sim 9.1$  Gyr stellar population of FRB 20200120E (Kirsten et al. 2021a).

The broad family of delayed channels is flexible in producing magnetars across a wide range of timescales, thus resulting in diverse host galaxy demographics (Nicholl et al. 2017; Margalit et al. 2019). However, for each of these channels that (in part) trace the host stellar mass, some fraction of FRBs should *also* appear in quiescent galaxies. In general, for progenitors that trace stellar mass alone, the FRB host galaxy demographics should reflect the universe’s stellar mass budget, which is roughly 1:1 in quiescent and SF galaxies at  $z \lesssim 0.5$  (Bell et al. 2003; Ilbert et al. 2010). For instance, a substantial fraction of the host galaxies of short-duration gamma-ray bursts (derived from NS mergers) and Type Ia SNe (derived from WD progenitors) are quiescent (Sullivan et al. 2006; Fong et al. 2017). Although there are now only seven known repeating FRBs with identified hosts to date, the lack of any quiescent host galaxy among this host population to date indicates that delayed channels are likely not responsible for all repeating FRBs, or that there is some uncharacterized bias against detecting repeating FRBs in quiescent, old stellar populations. However, the fact that a few repeating FRB hosts fall below the star-forming main sequence (Bhandari et al. 2021), coupled with the old local environment of FRB 20200120E, also indicates that recent or ongoing SF is not playing a dominant role in the production of FRBs.

## 5. Summary

We have presented the ASKAP localization of the bright, repeating FRB 20201124A source, as well as detailed observations and modeling of its host galaxy at  $z = 0.0979$ . Compared to the host properties of the FRB population, we find that the host galaxy is modestly star-forming ( $\sim 2\text{--}6 M_{\odot} \text{ yr}^{-1}$ ), moderately massive ( $\sim 2 \times 10^{10} M_{\odot}$ ), dusty ( $\sim 1\text{--}1.5$  mag of attenuation at optical wavelengths), and has a substantial stellar population (mass-weighted) age ( $\sim 5\text{--}6$  Gyr). We also find that the host has a somewhat low stellar metallicity of  $\sim (0.1\text{--}0.3)Z_{\odot}$ . The properties of the host place it among the population of normal star-forming galaxies at  $z \sim 0.1$  in terms of star formation, stellar mass, and gas-phase metallicity. The higher stellar mass of the host of FRB 20201124A is commensurate with its elevated SFR, and the specific SFR is unremarkable compared to the repeating FRB host population. Modeling the star formation and mass assembly histories, there is no clear evidence for any starburst activity, and most of the galaxy’s stellar mass was built prior to 1 Gyr ago. We further find that the primary source of the reported persistent radio

emission is recent star formation, as opposed to strong AGN activity.

FRB 20201124A marks the fifth extragalactic repeating FRB with an identified host galaxy. Notably, *all* identified hosts of known repeating FRBs exhibit modest amounts of ongoing star formation. However, no repeating FRB yet is localized to a quiescent galaxy, and several repeating FRB hosts are forming stars at a lower rate than field galaxies of the same stellar mass, indicating that ongoing SF is also not playing a dominant role in the FRB rate. This study demonstrates the advantage of using complementary tools—host galaxy demographics, local environments, and now star formation histories—to decipher the progenitors of FRBs. In particular, building the histories of these host galaxies provides an important view beyond the “present-day” snapshots afforded by more traditional stellar population modeling. Moreover, given the fairly sudden onset of activity of the FRB 20201124A source, as well as its brightness, it will be particularly insightful to connect the context clues learned from environments to the diversity of observed repeating FRB behaviors.

We thank MMT Observatory staff Benjamin Weiner and Skyler Self for rapidly scheduling and executing key observations. We thank Ron Ekers, Brian Metzger, and Sergio Campana for clarifying discussions. The Fast and Fortunate for FRB Follow-up team acknowledges support by the National Science Foundation under grant Nos. AST-1911140 and AST-1910471. The Fong Group at Northwestern acknowledges support by the National Science Foundation under grant Nos. AST-1814782, AST-1909358 and CAREER grant No. AST-2047919. R.M.S. acknowledges support through ARC Future Fellowship FT190100155. A.T.D. is the recipient of an Australian Research Council Future Fellowship (FT150100415). N.T. acknowledges support by FONDECYT grant 11191217. This research was partially supported by the Australian Government through the Australian Research Council’s Discovery Projects funding scheme (project DP210102103).

MMT Observatory access was supported by Northwestern University and the Center for Interdisciplinary Exploration and Research in Astrophysics (CIERA). Observations reported here were obtained at the MMT Observatory, a joint facility of the University of Arizona and the Smithsonian Institution. This work made use of data supplied by the UK Swift Science Data Centre at the University of Leicester. This research was supported in part through the computational resources and staff contributions provided for the Quest high performance computing facility at Northwestern University, which is jointly supported by the Office of the Provost, the Office for Research, and Northwestern University Information Technology. The National Radio Astronomy Observatory is a facility of the National Science Foundation operated under cooperative agreement by Associated Universities, Inc. The Australian SKA Pathfinder is part of the Australia Telescope National Facility, which is managed by CSIRO. Operation of ASKAP is funded by the Australian Government with support from the National Collaborative Research Infrastructure Strategy. ASKAP uses the resources of the Pawsey Supercomputing Centre. Establishment of ASKAP, the Murchison Radio-astronomy Observatory and the Pawsey Supercomputing Centre are initiatives of the Australian Government, with support from the Government of Western Australia and the

Science and Industry Endowment Fund. We acknowledge the Wajarri Yamatji people as the traditional owners of the Observatory site.

*Facilities:* MMT (Binospec), ASKAP, VLA, Swift (XRT).

*Software:* HEASOFT software (v.6.26; Blackburn et al. 1999; NASA High Energy Astrophysics Science Archive Research Center (HEASARC), 2014), *Prospector* (Leja et al. 2017), *Python-fsps* (Conroy et al. 2009; Conroy & Gunn 2010), *Dynesty* (Speagle 2020), *PyPeIt* (Prochaska et al. 2020).

## Appendix

### Prospector Stellar Population Modeling Description

Here, we describe the details of our *Prospector* stellar population modeling parameter definitions, priors, and assumptions. We initialize our stellar population models with a Chabrier IMF (Chabrier 2003) and Milky Way attenuation law (Cardelli et al. 1989) and further impose a few priors on the fit. First, we employ two wavelength- and age-dependent dust screens to represent (a) the attenuation by dust of stellar birth clouds, which affects only young stars (*dust1* in *Prospector*), and (b) the attenuation by dust of the diffuse ISM, which affects both young and old stars (*dust2* in *Prospector*). We assume a transition time between our designation of “young” and “old” stars of  $10^7$  yr (Conroy 2013) and impose a 2:1 ratio on the amount of dust attenuation between the younger and older stellar populations, as young stars in SF regions typically experience twice the amount of dust attenuation as older stars (Calzetti et al. 2000; Price et al. 2014). We additionally impose that the posteriors roughly adhere to the mass–metallicity ( $M_*-Z$ ) relationship (Gallazzi et al. 2005) at the relevant redshift. We employ a sixth-order Chebyshev polynomial to fit the spectral continuum.

We fix the redshift to  $z=0.0979$  and determine posteriors for all other free parameters, which include the total mass formed of stars from dust over the lifetime of the galaxy ( $M_F$ ), the lookback time at which star formation commences in the frame of the FRB host ( $t_{\max}$ , also corresponding to the maximum age), the stellar and gas-phase metallicities ( $Z_*$ ,  $Z_{\text{gas}}$ ), the  $e$ -folding time  $\tau$  in the assumed delayed- $\tau$  star formation history (SFH), and dust attenuation. We further use the samples of  $\tau$  and  $M_F$  to calculate the posteriors of the present-day stellar mass ( $M_*$ ), mass-weighted age ( $t_m$ ), SFR, and  $A_V$  using analytic conversions (Leja et al. 2013; Nugent et al. 2020). For fits with mid-IR components,  $f_{\text{AGN}}$  represents the fraction of the bolometric luminosity contribution from the AGN, and  $\tau_{\text{AGN}}$  is the optical depth of the dust torus. The assumed priors on these properties are listed in Table A1. To test how the results are affected by some of our input assumptions, we perform two additional fits with a delayed- $\tau$  SFH: one using the Calzetti attenuation law (Calzetti et al. 2000), which is broadly applicable to SF galaxies, and one that includes a mid-IR AGN component. For a fit that includes the mid-IR AGN contribution, we find a fraction of AGN contribution to the total flux of  $\sim 6\%$ , and its inclusion has little effect on the other derived properties.

For the nonparametric SFH fit, we include several additional spectroscopic calibration parameters and a flexible dust attenuation law following the model in Section 4.3 and Table 2 of Johnson et al. (2021). We describe the SFH with eight bins in lookback time, two spaced at 0–30 Myr and 30–100 Myr and the remaining six spaced evenly in logarithmic time, with the upper limit set to be the age of the universe at the observed

**Table A1**  
Prior Ranges for *Prospector* Fitting

Property	Range
$\log(M_F/M_\odot)$	[8, 12]
$\log(r_i)$	[−100, 100] <sup>b</sup>
$t_{\text{age}}^a$ (Gyr)	[0, 12.4]
$\tau^a$ (Gyr)	[0.1, 10]
$\log(Z_*/Z_\odot)$	[−2.0, 0.19]
$\log(Z_{\text{gas}}/Z_\odot)$	[−2, 0.5]
<i>dust1</i> / <i>dust2</i>	[0, 1.5]
<i>dust2</i>	[0, 4]
$f_{\text{AGN}}$	[ $10^{-5}$ , 3.0]
$\tau_{\text{AGN}}$	[5.0, 150.0]





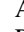
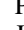

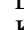
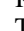







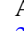


#### Notes.

<sup>a</sup> For parametric SFH fits only.

<sup>b</sup> For nonparametric SFH fits only.

redshift. These are characterized by the parameter  $r_i$  in the fit, which represents the ratio of the SFR in temporal bin  $i$  to that in the adjacent bin. A continuity prior is adopted for the SFH (Leja et al. 2019), which weights against strong changes in the SFR with time and prefers a constant SFR in the absence of data. Thus, any deviation from a flat star formation history in the results will be driven by the data and not the priors. In this fit, we also include a mid-IR AGN component. The priors are listed in Table A1.

## ORCID iDs

Wen-fai Fong  <https://orcid.org/0000-0002-7374-935X>  
Yuxin Dong  <https://orcid.org/0000-0002-9363-8606>  
Joel Leja  <https://orcid.org/0000-0001-6755-1315>  
Shivani Bhandari  <https://orcid.org/0000-0003-3460-506X>  
Cherie K. Day  <https://orcid.org/0000-0002-8101-3027>  
Adam T. Deller  <https://orcid.org/0000-0001-9434-3837>  
Pravir Kumar  <https://orcid.org/0000-0003-1913-3092>  
J. Xavier Prochaska  <https://orcid.org/0000-0002-7738-6875>  
Danica R. Scott  <https://orcid.org/0000-0002-6895-4156>  
Keith W. Bannister  <https://orcid.org/0000-0003-2149-0363>  
Tarraneh Eftekhari  <https://orcid.org/0000-0003-0307-9984>  
Alexa C. Gordon  <https://orcid.org/0000-0002-5025-4645>  
Kasper E. Heintz  <https://orcid.org/0000-0002-9389-7413>  
Clancy W. James  <https://orcid.org/0000-0002-6437-6176>  
Charles D. Kilpatrick  <https://orcid.org/0000-0002-5740-7747>  
Elizabeth K. Mahony  <https://orcid.org/0000-0002-5053-2828>  
Alicia Rouco Escorial  <https://orcid.org/0000-0003-3937-0618>  
Stuart D. Ryder  <https://orcid.org/0000-0003-4501-8100>  
Ryan M. Shannon  <https://orcid.org/0000-0002-7285-6348>  
Nicolas Tejos  <https://orcid.org/0000-0002-1883-4252>

## References

- Aggarwal, K., Budavári, T., Deller, A. T., et al. 2021, *ApJ*, 911, 95  
Ahumada, R., Prieto, C. A., Almeida, A., et al. 2020, *ApJS*, 249, 3  
Baldwin, J. A., Phillips, M. M., & Terlevich, R. 1981, *PASP*, 93, 5  
Bannister, K., Zackay, B., Qiu, H., James, C., & Shannon, R. 2019a, FREDDA: A fast, real-time engine for de-dispersing amplitudes, *Astrophysics Source Code Library*, ascl:1906.003  
Bannister, K. W., Deller, A. T., Phillips, C., et al. 2019b, *Sci*, 365, 565  
Bassa, C. G., Tendulkar, S. P., Adams, E. A. K., et al. 2017, *ApJL*, 843, L8

- Beck, R., Szapudi, I., Flewelling, H., et al. 2021, *MNRAS*, **500**, 1633
- Bell, E. F., McIntosh, D. H., Katz, N., & Weinberg, M. D. 2003, *ApJS*, **149**, 289
- Bennett, C. L., Larson, D., Weiland, J. L., & Hinshaw, G. 2014, *ApJ*, **794**, 135
- Berger, E. 2010, *ApJ*, **722**, 1946
- Bertin, E., & Arnouts, S. 1996, *A&AS*, **117**, 393
- Bhandari, S., Sadler, E. M., Prochaska, J. X., et al. 2020a, *ApJL*, **895**, L37
- Bhandari, S., Bannister, K. W., Lenc, E., et al. 2020b, *ApJL*, **901**, L20
- Bhandari, S., Heintz, K. E., Aggarwal, K., et al. 2021, arXiv:2108.01282
- Bhardwaj, M., Gaensler, B. M., Kaspi, V. M., et al. 2021a, *ApJL*, **910**, L18
- Bhardwaj, M., Kirichenko, A. Yu., Michilli, D., et al. 2021b, arXiv:2108.12122
- Blackburn, J. K., Shaw, R. A., Payne, H. E., Hayes, J. J. E. & HEASARC 1999, FTOOLS: A general package of software to manipulate FITS files, Astrophysics Source Code Library, ascl:9912.002
- Bloom, J. S., Kulkarni, S. R., & Djorgovski, S. G. 2002, *AJ*, **123**, 1111
- Bochenek, C. D., Ravi, V., Belov, K. V., et al. 2021, *Natur*, **587**, 59
- Bochenek, C. D., Ravi, V., & Dong, D. 2021, *ApJL*, **907**, L31
- Brinchmann, J., Pettini, M., & Charlot, S. 2008, *MNRAS*, **385**, 769
- Calzetti, D., Armus, L., Bohlin, R. C., et al. 2000, *ApJ*, **533**, 682
- Campana, S. 2021, *ATel*, **14523**, 1
- Cardelli, J. A., Clayton, G. C., & Mathis, J. S. 1989, *ApJ*, **345**, 245
- Castrillo, A., Ascasibar, Y., Galbany, L., et al. 2021, *MNRAS*, **501**, 3122
- Chabrier, G. 2003, *PASP*, **115**, 763
- Chambers, K. C., Magnier, E. A., Metcalfe, N., et al. 2016, arXiv:1612.05560
- Chatterjee, S., Law, C. J., Wharton, R. S., et al. 2017, *Natur*, **541**, 58
- CHIME/FRB Collaboration 2021a, *ATel*, **14497**, 1
- CHIME/FRB Collaboration 2021b, *TNSFR* **2021-990**
- CHIME/FRB Collaboration, Andersen, B. C., Bandura, K., et al. 2019, *ApJL*, **885**, L24
- CHIME/FRB Collaboration, Andersen, B. C., Bandura, K. M., et al. 2020, *Natur*, **587**, 54
- Chrimas, A. A., Levan, A. J., Groot, P. J., Lyman, J. D., & Nelemans, G. 2021, arXiv:2105.04549
- Condon, J. J. 1980, *ApJ*, **242**, 894
- Condon, J. J. 1992, *ARA&A*, **30**, 575
- Conroy, C. 2013, *ARA&A*, **51**, 393
- Conroy, C., & Gunn, J. E. 2010, *ApJ*, **712**, 833
- Conroy, C., Gunn, J. E., & White, M. 2009, *ApJ*, **699**, 486
- Cordes, J. M., & Chatterjee, S. 2019, *ARA&A*, **57**, 417
- Cordes, J. M., & Lazio, T. J. W. 2002, arXiv:astro-ph/0207156
- Cutri, R. M., Wright, E. L., Conrow, T., et al. 2021, *yCat*, **2328**, 0
- Day, C. K., Bhandari, S., Deller, A. T., Shannon, R. M. & ASKAP-CRAFT Survey Science Project 2021a, *ATel*, **14592**, 1
- Day, C. K., Bhandari, S., Deller, A. T., Shannon, R. M., & Moss, V. A. 2021b, *ATel*, **14515**, 1
- Day, C. K., Deller, A. T., James, C. W., et al. 2021c, arXiv:2107.07068
- Day, C. K., Deller, A. T., Shannon, R. M., et al. 2020, *MNRAS*, **497**, 3335
- de Blok, W. J. G., Walter, F., Brinks, E., et al. 2008, *AJ*, **136**, 2648
- Duncan, R. C., & Thompson, C. 1992, *ApJ*, **392**, L9
- Eftekhari, T., Berger, E., Margalit, B., et al. 2019, *ApJL*, **876**, L10
- Ekers, R. D., & Shakeshaft, J. R. 1974, in *IAU Symp. 58, The Formation and Dynamics of Galaxies*, ed. J. R. Shakeshaft (Dordrecht: Reidel), 257
- Fabricant, D., Fata, R., Epps, H., et al. 2019, *PASP*, **131**, 075004
- Fang, J. J., Faber, S. M., Koo, D. C., et al. 2018, *ApJ*, **858**, 100
- Farah, W., Pollak, A. W., Siemion, A. P. V., et al. 2021, *ATel*, **14676**, 1
- Fitzpatrick, E. L., & Massa, D. 2007, *ApJ*, **663**, 320
- Fong, W., Berger, E., Blanchard, P. K., et al. 2017, *ApJL*, **848**, L23
- Fonseca, E., Andersen, B. C., Bhardwaj, M., et al. 2020, *ApJL*, **891**, L6
- Fumagalli, M., Labbé, I., Patel, S. G., et al. 2014, *ApJ*, **796**, 35
- Gajjar, V., Siemion, A. P. V., Price, D. C., et al. 2018, *ApJ*, **863**, 2
- Galbany, L., Anderson, J. P., Rosales-Ortega, F. F., et al. 2016, *MNRAS*, **455**, 4087
- Gallazzi, A., Charlot, S., Brinchmann, J., White, S. D. M., & Tremonti, C. A. 2005, *MNRAS*, **362**, 41
- Gehrels, N. 1986, *ApJ*, **303**, 336
- Gehrels, N., Chincarini, G., Giommi, P., et al. 2004, *ApJ*, **611**, 1005
- Gordon, K. D., Pérez-González, P. G., Misselt, K. A., et al. 2004, *ApJS*, **154**, 215
- Groves, B., Krause, O., Sandstrom, K., et al. 2012, *MNRAS*, **426**, 892
- Hao, C.-N., Kennicutt, R. C., Johnson, B. D., et al. 2011, *ApJ*, **741**, 124
- Hatsukade, B., Tominaga, N., Hayashi, M., et al. 2018, *ApJ*, **857**, 72
- Heintz, K. E., Prochaska, J. X., Simha, S., et al. 2020, *ApJ*, **903**, 152
- Herrmann, W. 2021, *ATel*, **14556**, 1
- Heywood, I., Camilo, F., Cotton, W. D., et al. 2019, *Natur*, **573**, 235
- Hirschauer, A. S., Salzer, J. J., Janowiecki, S., & Wegner, G. A. 2018, *AJ*, **155**, 82
- Ilbert, O., Salvato, M., Le Floc'h, E., et al. 2010, *ApJ*, **709**, 644
- Ishibashi, W., & Courvoisier, T. J. L. 2010, *A&A*, **512**, A58
- Johnson, B. D., Leja, J., Conroy, C., & Speagle, J. S. 2021, *ApJS*, **254**, 22
- Kashiyama, K., & Murase, K. 2017, *ApJL*, **839**, L3
- Kelly, P. L., & Kirshner, R. P. 2012, *ApJ*, **759**, 107
- Kennicutt, R. C., Jr. 1998, *ARA&A*, **36**, 189
- Kilpatrick, C. D., Fong, W., Prochaska, J. X., et al. 2021, *ATel*, **14516**, 1
- Kirsten, F., Marcote, B., Nimmo, K., et al. 2021a, arXiv:2105.11445
- Kirsten, F., Ould-Boukattine, O. S., Nimmo, K., et al. 2021b, *ATel*, **14605**, 1
- Kremer, K., Ye, C. S., Chatterjee, S., Rodriguez, C. L., & Rasio, F. A. 2020, in *IAU Symp. 351, Star Clusters: From the Milky Way to the Early Universe*, ed. A. Bragaglia et al. (Cambridge: Cambridge Univ. Press), 357
- Kumar, P., Shannon, R. M., Keane, E., Moss, V. A. & Askap-Craft Survey Science Project 2021a, *ATel*, **14508**, 1
- Kumar, P., Shannon, R. M., Moss, V., Qiu, H., & Bhandari, S. 2021b, *ATel*, **14502**, 1
- Law, C., Tendulkar, S., Clarke, T., Aggarwal, K., & Bethapudy, S. 2021, *ATel*, **14526**, 1
- Leja, J., Carnall, A. C., Johnson, B. D., Conroy, C., & Speagle, J. S. 2019, *ApJ*, **876**, 3
- Leja, J., Johnson, B. D., Conroy, C., Dokkum, P. G. v., & Byler, N. 2017, *ApJ*, **837**, 170
- Leja, J., Johnson, B. D., Conroy, C., & van Dokkum, P. 2018, *ApJ*, **854**, 62
- Leja, J., van Dokkum, P. G., Momcheva, I., et al. 2013, *ApJL*, **778**, L24
- Levesque, E. M., Berger, E., Kewley, L. J., & Bagley, M. M. 2010, *AJ*, **139**, 694
- Li, D., Niu, C. H., Aggarwal, K., et al. 2021, *Nature Portfolio*, doi:10.21203/rs.3.rs-745622/v1
- Li, Y., & Zhang, B. 2020, *ApJL*, **899**, L6
- Licquia, T. C., & Newman, J. A. 2015, *ApJ*, **806**, 96
- Lorimer, D. R., Bailes, M., McLaughlin, M. A., Narkevic, D. J., & Crawford, F. 2007, *Sci*, **318**, 777
- Lunnan, R., Chornock, R., Berger, E., et al. 2014, *ApJ*, **787**, 138
- Macquart, J.-P., Bailes, M., Bhat, N. D. R., et al. 2010, *PASA*, **27**, 272
- Macquart, J. P., Prochaska, J. X., McQuinn, M., et al. 2020, *Natur*, **581**, 391
- Magnier, E. A., Schlafly, E. F., Finkbeiner, D. P., et al. 2020, *ApJS*, **251**, 6
- Mahony, E. K., Ekers, R. D., Macquart, J.-P., et al. 2018, *ApJL*, **867**, L10
- Maiolino, R., Nagao, T., Grazian, A., et al. 2008, *A&A*, **488**, 463
- Mannings, A. G., Fong, W.-f., Simha, S., et al. 2021, *ApJ*, **917**, 75
- Marcote, B., Nimmo, K., Hessels, J. W. T., et al. 2020, *Natur*, **577**, 190
- Marcote, B., Kirsten, F., Hessels, J. W. T., et al. 2021, *ATel*, **14603**, 1
- Margalit, B., Berger, E., & Metzger, B. D. 2019, *ApJ*, **886**, 110
- Margalit, B., & Metzger, B. D. 2018, *ApJL*, **868**, L4
- Marthi, V. R., Bethapudi, S., Main, R. A., et al. 2021, arXiv:2108.00697
- McMillan, P. J. 2011, *MNRAS*, **414**, 2446
- Metzger, B. D., Berger, E., & Margalit, B. 2017, *ApJ*, **841**, 14
- Metzger, B. D., Margalit, B., Kasen, D., & Quataert, E. 2015, *MNRAS*, **454**, 3311
- Michilli, D., Seymour, A., Hessels, J. W. T., et al. 2018, *Natur*, **553**, 182
- Molnár, D. C., Sargent, M. T., Leslie, S., et al. 2021, *MNRAS*, **504**, 118
- Moustakas, J., Kennicutt, R. C., Jr., & Tremonti, C. A. 2006, *ApJ*, **642**, 775
- Murphy, E. J., Condon, J. J., Schinnerer, E., et al. 2011, *ApJ*, **737**, 67
- NASA High Energy Astrophysics Science Archive Research Center (HEASARC) 2014, HEASoft: Unified Release of FTOOLS and XANADU, Astrophysics Source Code Library, ascl:1408.004
- Nicholl, M., Williams, P. K. G., Berger, E., et al. 2017, *ApJ*, **843**, 84
- Nugent, A. E., Fong, W., Dong, Y., et al. 2020, *ApJ*, **904**, 52
- O'Connor, B., Piro, L., Lotti, S., et al. 2021, *ATel*, **14525**, 1
- Osterbrock, D. E., & Ferland, G. J. 1989, *Astrophysics of Gaseous Nebulae and Active Galactic Nuclei* (Sausalito, CA: Univ. Science Books)
- Panessa, F., Baldi, R. D., Laor, A., et al. 2019, *NatAs*, **3**, 387
- Perley, D. A., Perley, R. A., Hjorth, J., et al. 2015, *ApJ*, **801**, 102
- Perley, D. A., Quimby, R. M., Yan, L., et al. 2016, *ApJ*, **830**, 13
- Petroff, E., Hessels, J. W. T., & Lorimer, D. R. 2019, *A&ARv*, **27**, 4
- Piro, L., Bruni, G., Troja, E., et al. 2021, arXiv:2107.14339
- Platts, E., Weltman, A., Walters, A., et al. 2019, *PhRv*, **821**, 1
- Pleunis, Z., Good, D. C., Kaspi, V. M., et al. 2021, arXiv:2106.04356
- Price, S. H., Kriek, M., Brammer, G. B., et al. 2014, *ApJ*, **788**, 86
- Prochaska, J., Hennawi, J., Westfall, K., et al. 2020, *JOSS*, **5**, 2308
- Prochaska, J. X., & Zheng, Y. 2019, *MNRAS*, **485**, 648
- Ravi, V., Law, C. J., Li, D., et al. 2021, arXiv:2106.09710
- Raynaud, R., Guilet, J., Janka, H.-T., & Gastine, T. 2020, *SciA*, **6**, eaay2732
- Ricci, R., Piro, L., Panessa, F., et al. 2021, *ATel*, **14549**, 1

- Safarzadeh, M., Prochaska, J. X., Heintz, K. E., & Fong, W.-f. 2020, *ApJL*, **905**, L30
- Savaglio, S., Glazebrook, K., & Le Borgne, D. 2009, *ApJ*, **691**, 182
- Schulze, S., Yaron, O., Sollerman, J., et al. 2021, *ApJS*, **255**, 29
- Shang, Z., Brotherton, M. S., Wills, B. J., et al. 2011, *ApJS*, **196**, 2
- Shannon, R. M., Macquart, J. P., Bannister, K. W., et al. 2018, *Natur*, **562**, 386
- Skrutskie, M. F., Cutri, R. M., Stiening, R., et al. 2006, *AJ*, **131**, 1163
- Speagle, J. S. 2020, *MNRAS*, **493**, 3132
- Spitler, L. G., Scholz, P., Hessels, J. W. T., et al. 2016, *Natur*, **531**, 202
- Sullivan, M., Le Borgne, D., Pritchett, C. J., et al. 2006, *ApJ*, **648**, 868
- Tendulkar, S. P., Bassa, C. G., Cordes, J. M., et al. 2017, *ApJL*, **834**, L7
- Tendulkar, S. P., Gil de Paz, A., Kirichenko, A. Y., et al. 2021, *ApJL*, **908**, L12
- Terashima, Y., & Wilson, A. S. 2003, *ApJ*, **583**, 145
- The CHIME/FRB Collaboration, Amiri, M., et al. 2021, arXiv:2106.04352
- Theios, R. L., Steidel, C. C., Strom, A. L., et al. 2019, *ApJ*, **871**, 128
- Thornton, D., Stappers, B., Bailes, M., et al. 2013, *Sci*, **341**, 53
- Tremonti, C. A., Heckman, T. M., Kauffmann, G., et al. 2004, *ApJ*, **613**, 898
- Vergani, S. D., Salvaterra, R., Japelj, J., et al. 2015, *A&A*, **581**, A102
- Viaene, S., Baes, M., Tamm, A., et al. 2017, *A&A*, **599**, A64
- Watson, D. 2011, *A&A*, **533**, A16
- Wharton, R., Bethapudi, S., Marthi, V., et al. 2021a, ATel, **14538**, 1
- Wharton, R., Bethapudi, S., Gautam, T., et al. 2021b, ATel, **14529**, 1
- Whitaker, K. E., van Dokkum, P. G., Brammer, G., & Franx, M. 2012, *ApJL*, **754**, L29
- Williams, R. J., Quadri, R. F., Franx, M., van Dokkum, P., & Labbé, I. 2009, *ApJ*, **691**, 1879
- Willingale, R., Starling, R. L. C., Beardmore, A. P., Tanvir, N. R., & O'Brien, P. T. 2013, *MNRAS*, **431**, 394
- Willmer, C. N. A., Faber, S. M., Koo, D. C., et al. 2006, *ApJ*, **647**, 853
- Wright, E. L., Eisenhardt, P. R. M., Mainzer, A. K., et al. 2010, *AJ*, **140**, 1868
- Wu, X.-B., Hao, G., Jia, Z., Zhang, Y., & Peng, N. 2012, *AJ*, **144**, 49
- Xu, H., Niu, J., Lee, K., et al. 2021, ATel, **14518**, 1
- Yun, M. S., & Carilli, C. L. 2002, *ApJ*, **568**, 88
- Yusef-Zadeh, F., Hewitt, J. W., & Cotton, W. 2004, *ApJS*, **155**, 421
- Zackay, B., & Ofek, E. O. 2017, *ApJ*, **835**, 11
- Zapartas, E., de Mink, S. E., Izzard, R. G., et al. 2017, *A&A*, **601**, A29